



## OPEN ACCESS

## EDITED BY

Cristina De Campos,  
Ludwig Maximilian University of Munich,  
Germany

## REVIEWED BY

Ciro Ávila,  
Federal University of Rio de Janeiro,  
Brazil  
Adriana Alves,  
University of São Paulo, Brazil

## \*CORRESPONDENCE

Ashima Saikia,  
ashima.saikia@gmail.com

## SPECIALTY SECTION

This article was submitted to Petrology,  
a section of the journal  
Frontiers in Earth Science

RECEIVED 25 May 2022

ACCEPTED 29 July 2022

PUBLISHED 02 September 2022

## CITATION

Negi P, Saikia A, Ahmad M, Upadhyay D  
and Akhtar S (2022), Nature and origin of  
anorthosite enclaves within Proterozoic  
granite of Chotanagpur Granite Gneiss  
Complex of Eastern India.  
*Front. Earth Sci.* 10:952554.  
doi: 10.3389/feart.2022.952554

## COPYRIGHT

© 2022 Negi, Saikia, Ahmad, Upadhyay  
and Akhtar. This is an open-access  
article distributed under the terms of the  
[Creative Commons Attribution License  
\(CC BY\)](https://creativecommons.org/licenses/by/4.0/). The use, distribution or  
reproduction in other forums is  
permitted, provided the original  
author(s) and the copyright owner(s) are  
credited and that the original  
publication in this journal is cited, in  
accordance with accepted academic  
practice. No use, distribution or  
reproduction is permitted which does  
not comply with these terms.

# Nature and origin of anorthosite enclaves within Proterozoic granite of Chotanagpur Granite Gneiss Complex of Eastern India

Priyanka Negi<sup>1</sup>, Ashima Saikia<sup>1\*</sup>, Mansoor Ahmad<sup>2</sup>,  
Dewashis Upadhyay<sup>3</sup> and Salim Akhtar<sup>1</sup>

<sup>1</sup>Department of Geology, University of Delhi, Delhi, India, <sup>2</sup>Geological Survey of India, SU, Jharkhand, India, <sup>3</sup>Department of Geology and Geophysics, Indian Institute of Technology, Kharagpur, West Bengal, India

The Central Indian Tectonic Zone (CITZ) is a Proterozoic suture along which the Northern and Southern Indian Blocks are inferred to have amalgamated, forming the Greater Indian Landmass. The Chotanagpur Granite Gneiss Complex (CGGC) represents the eastern extension of the CITZ and exposes several granite plutons. Enclaves of diverse origin are present as minor constituents within these granitic bodies. This study reports new major and trace element data for anorthosite enclaves hosted within granites in the Pattharkatti and Rajgir area from the northern margin of CGGC to get modern insights into the petrogenesis of anorthosites. Anorthosite enclaves show sharp contact with the host granite. They contain cumulus plagioclase (An<sub>87–94</sub>), intercumulus amphibole (magnesiohornblende and ferrotschermakite), and biotite (Mg-biotite and phlogopite) along with minor iron oxides. Amphibole crystallization pressure and temperature are constrained between 0.5 and 6.4 kbar and 653–780°C for the anorthosites. The studied anorthosites display a very gradual and steady increase in whole-rock rare earth element (REE) contents from Lu to La [(La/Yb)<sub>N</sub> = 1.22–13.08]. They also show a sharp decline in Fe<sub>2</sub>O<sub>3</sub>(t) and MgO, whereas Al<sub>2</sub>O<sub>3</sub> increases with increasing silica contents from 45.69 to 51.16 wt%. In the chondrite normalized REE diagram, plagioclase exhibits LREE enriched patterns with strong positive Eu anomaly. The composition of parental liquid for anorthosite from the study area was estimated by adopting the equilibrium distribution method. Parental melt curves from Sm to La are near parallel and constrained broadly between trapped melt fractions (TMF) = ~5%–15%. Anorthosites of the study area may have formed from the plagioclase-saturated basaltic melt.

## KEYWORDS

enclaves, Chotanagpur Granite Gneiss Complex, anorthosite, hornblendite, pyroxenite

## 1 Introduction

Enclaves are fragments of foreign rocks comprising one individual crystal or an aggregate of crystals enclosed in homogeneous igneous rock (Didier and Barbarin, 1991). Enclaves have diverse characteristics, implications, and origins. As enclaves are embedded within a plutonic rock, they may be older or contemporaneous with the host. Based on the diverse mineralogy, composition, and textures, Didier and Barbarin (1991) proposed nomenclature for four major types of enclaves: surmicaceous, schlieren, xenolith, and magmatic. Magmatic enclaves are the most common and abundant in granite hosts. These enclaves are widely distributed throughout a pluton and vary in abundance at the outcrop level (Vernon, 1984; Wiebe et al., 1997).

Several hypotheses exist regarding the origin of magmatic enclaves. One widely held view is that they are generated by mixing or mingling mafic and crustal felsic magmas (Vernon, 1984; Frost and Mahood, 1987; Dorais et al., 1990; Blundy and Sparks, 1992; Wiebe et al., 1997; Perugini et al., 2003; Barbarin, 2005; Feeley et al., 2008). The “Restite Model,” which is an alternative idea, considers magmatic enclaves as refractory solid residues of partial melting of a source (e.g., White and Chappell, 1977; Chappell et al., 1987; Chen et al., 1989; Chappell, 1996; White et al., 1999; Chappell et al., 2000). A third proposition, known as the “Cognate Model,” considers magmatic enclaves as an accumulation of early crystallized minerals from the magma or a cogenetic melt and trapped interstitial liquids (e.g., Fershtater and Borodina, 1977; Phillips et al., 1981; Clemens and Wall, 1984; Clemens and Wall, 1988; Dodge and Kistler, 1990; Fershtater and Borodina, 1991; Dahlquist, 2002; Ilbeyli and Pearce, 2005). Three slightly different mechanisms have been proposed under the “Cognate Model” for forming enclaves: 1) cumulate clots (Dodge and Kistler, 1990; Dahlquist, 2002), 2) disrupted chilled margins (Donaire et al., 2005), and 3) disrupted cumulate assemblages (Bébin, 1991; Platevoet and Bonin, 1991). The different hypotheses described above reflect the complexity of enclave-forming processes and the lack of consensus on their origin. One major debate has been the identification of the parental magmas of magmatic enclaves.

The focus of this work is the petrochemical characterization of anorthosite enclaves hosted within Proterozoic granites of the Chotanagpur Granite Gneiss Complex (CGGC) to 1) document their geochemical composition, 2) constrain possible parental melt composition based on trace element modeling, and 3) ascertain their origin. In addition, enclaves of pyroxenite, hornblendite, and diorite, which are rare in the study area, are also characterized to explore any correlation with the anorthosites.

## 2 Geological setting

A roughly WNW–ESE–trending orogenic belt, called the Central Indian Tectonic Zone (CITZ) (Figure 1A), dissects the Indian shield into two halves and represents a major paleosuture along which different Archean and Paleoproterozoic blocks of the Indian shield are believed to have fused to form the “Greater Indian Landmass” (Acharyya, 2003; Bhowmik, 2019). The CGGC, which is a vast tract in the Peninsular Eastern Indian Shield, comprises gneisses, granites, and granulite-facies rocks (Ghose, 1992) and represents the eastern extension of the CITZ. It covers an area of 100,000 sq km in the Indian States of Chattisgarh, Jharkhand, Bihar, and West Bengal (e.g., Mahadevan, 2002; Acharyya, 2003; Sharma, 2009; Sanyal and Sengupta, 2012) (Figures 1A, B). The CGGC is juxtaposed between two mobile belts, namely, the North Singhbhum Mobile Belt in the south and the Mahakoshal Mobile Belt in the north (Figure 1B). It is also surrounded by the Gangetic alluvium in the north, the Mesozoic Rajmahal Traps in the east, and Gondwana deposits and supracrustal rocks and granitoids of the Mahakoshal Group in the west.

The CGGC is a complex collage of high-grade ortho- and para-gneisses, migmatites, and metasedimentary enclaves intruded by metabasic, anorthositic, and granitic plutons (Figure 1B) (Ghose, 1983; Mazumdar, 1988; Sarkar, 1988; Ghose, 1992). Younger mafic, ultramafic, and alkaline (sodic and ultrapotassic) intrusives of early Tertiary age are also present. The metasedimentary suite includes metapelite, quartzite, and calc-silicate rocks. The evolution of the CGGC is marked by multiple episodes of magmatism, metamorphism, and deformation over a geological history spanning from Proterozoic to approximately 65 Ma (Mukherjee and Ghose, 1998). Mukherjee et al. (2019) divided the CGGC into three roughly east–west domains. Domain IA covers rocks exposed in the southernmost part of the CGGC and is bounded by the Gondwana Boundary Fault (GBF) and the South Purulia Suture Zone (SPSZ). The E–W trending Domain IB is sandwiched between GBF and Domain II to its north. Domain II is sandwiched between Domain III in the north and the GBF in the south and includes the ENE–WSW trending Bihar Mica Belt (BMB), which comprises a distinct lithological ensemble in the CGGC. Domain III at the northern fringe of CGGC, north of the BMB, comprises migmatitic quartzo-feldspathic gneisses and supracrustals. The present study area (Figure 1B) lies in Domain III of Mukherjee et al. (2019). Overall, four magmato-metamorphic events, viz., >2.5 Ga, 1.6–1.5 Ga, 1.2–1.0 Ga, and 0.9 Ga, have been proposed for this crustal block by different workers, mainly based on zircon U–Pb ages (Chatterjee et al., 2008), whole-rock (WR) Rb–Sr isochron (Krishna et al., 1996; Singh and Krishna, 2009), and monazite

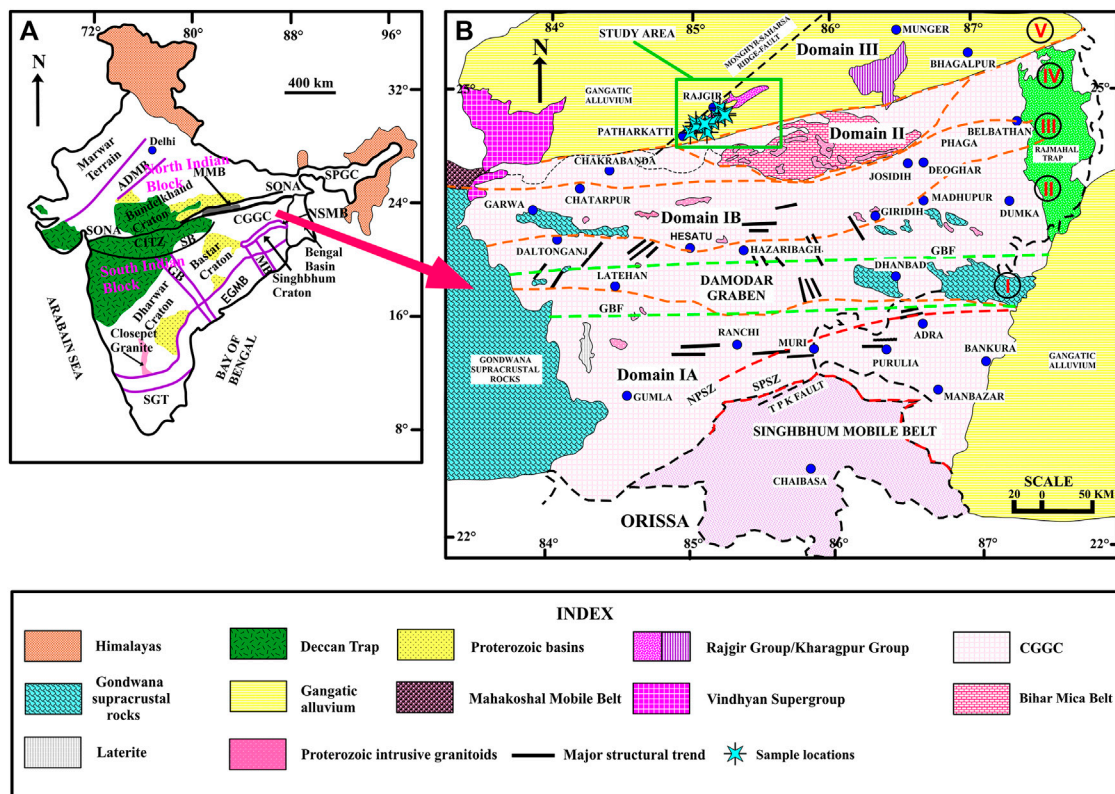


FIGURE 1

(A) map of India showing the location of the Central Indian Tectonic Zone (CITZ) along with other Proterozoic mobile belts of India, including the Eastern Ghats Mobile Belt and the Aravalli Delhi Mobile Belt. The CITZ comprises the central CITZ, the Chotanagpur Granite Gneiss Complex (CGGC), and the easternmost Shillong Plateau Gneissic Complex. Four Archaean cratonic nuclei of India, namely, Singhbhum, Bastar, Bundelkhand, and Dharwar, are also shown (modified after Pradhan et al., 2009). GB, Godavari Basin; MB, Mahanadi Basin; MMB, Mahakoshal Mobile Belt; SB, Satpura Basin; NSMB, North Singhbhum Mobile Belt; SGT, Southern Granulite Terrain. (B) map of CGGC modified after Sanyal and Sengupta 2012 showing the five subdivisions of CGGC, namely, (I) Ranchi–Purulia, (II) Hazaribagh–Dumka, (III) Giridih–Deoghar, (IV) Bihar Mica Belt, and (V) Rajgir–Kharagpur subdivisions as proposed by Mahadevan (2002) delineated by orange lines. Also shown in the map are current subdivisions of CGGC proposed by Mukherjee et al. (2019) marked as Domain I (IA and IB), Domain II, and Domain III. The green square box shows the study area. Sample locations are marked in stars. NPSZ, North Purulia Shear Zone; SPSZ, South Purulia Shear Zone.

chemical dates (Maji et al., 2008; Chatterjee et al., 2010; Karmakar et al., 2011). Most of these ages are from the metamorphosed basement lithologies in the eastern part of the high-grade terrain. Chatterjee and Ghose (2011) reported a crystallization age of  $1,697 \pm 17$  Ma (U–Pb monazite) of porphyritic granite from the northern margin of CGGC. Saikia et al. (2017) and Saikia et al. (2019) suggested subduction-related arc magmatism for the formation of the granites of the Bathani volcanic and volcano–sedimentary sequence emplaced at approximately 1,700–1,600 Ma.

The study area (Rajgir and Pattharkatti) (Figure 1B) falls in the northern part of the Chhotanagpur plateau, flanked by Indo–Gangetic alluvial plains in the north and the Rajgir Group of Proterozoic metasedimentary rocks in the southeast. The area exposes a gabbro–anorthosite–granite suite. The granites are of Proterozoic age (1,750–1,660 Ma;

U–Pb in zircon; Saikia et al., 2017). Enclaves of anorthosites are found within granites in the Rajgir area. The enclaves are either rounded or angular and of variable size (<0.5 m in the longer dimension) (Figures 2A–C). In the Pattharkatti area, exposures of granite plutons are observed, wherein anorthosites are seen hosted within the granites. In addition, pyroxenite and hornblende enclaves are hosted within the anorthosites (Figures 3A–C).

It is of interest that a diorite enclave was seen to occur within the anorthosite, which in turn was hosted within the granite (Figure 3D), representing a double enclave. Anorthosite enclaves are also observed hosted within the granite in the Pattharkatti area (Figure 4A). In addition, a dolerite dyke cross-cuts the same granite body (Figure 4B). These different rock enclaves display sharp margins with the host granites.

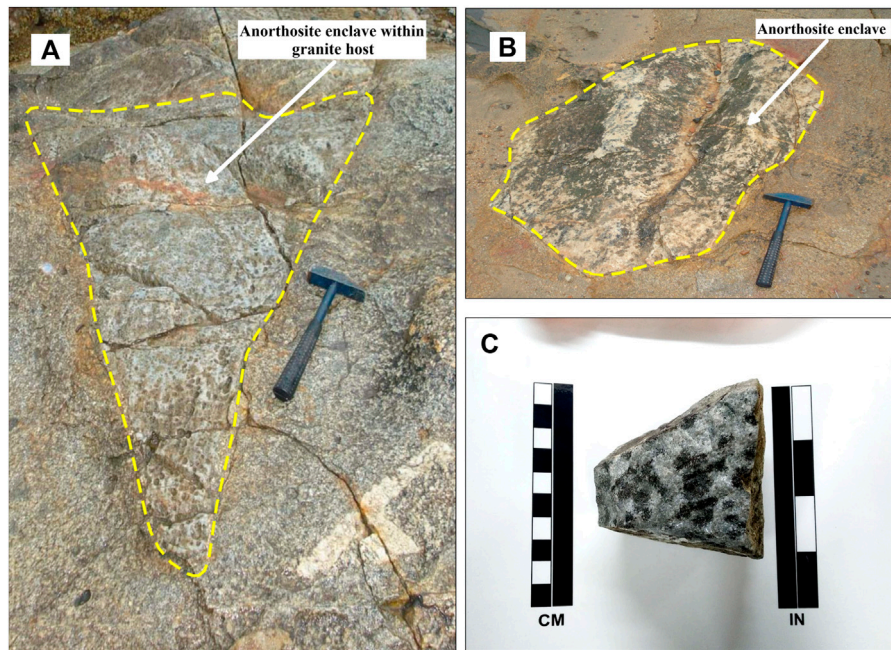


**FIGURE 2**  
**(A,B)** anorthosite enclaves within Proterozoic granite from the Rajgir locality (N 24°59'33.5", E 85°15'47.6") of northern CGGC. **(C)** a photograph of the hand specimen of anorthosite enclave.

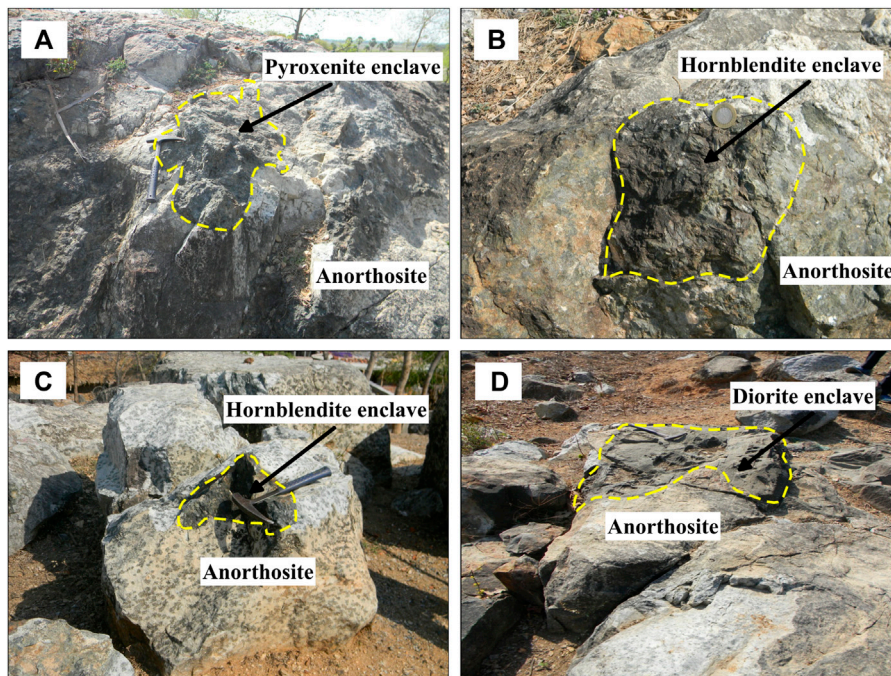


**FIGURE 3**  
 Different enclaves found within the anorthosites of the Pattarkatti region **(A)** pyroxenite enclave (N 24°58'99.0", E 85°12'08.22") **(B, C)** hornblende enclave (N 24°58'35.7", E 85°12'08.22"; N 24°58'99.0", E 85°12'08.22") **(D)** diorite enclave (N 24°58'99.0", E 85°12'08.22").

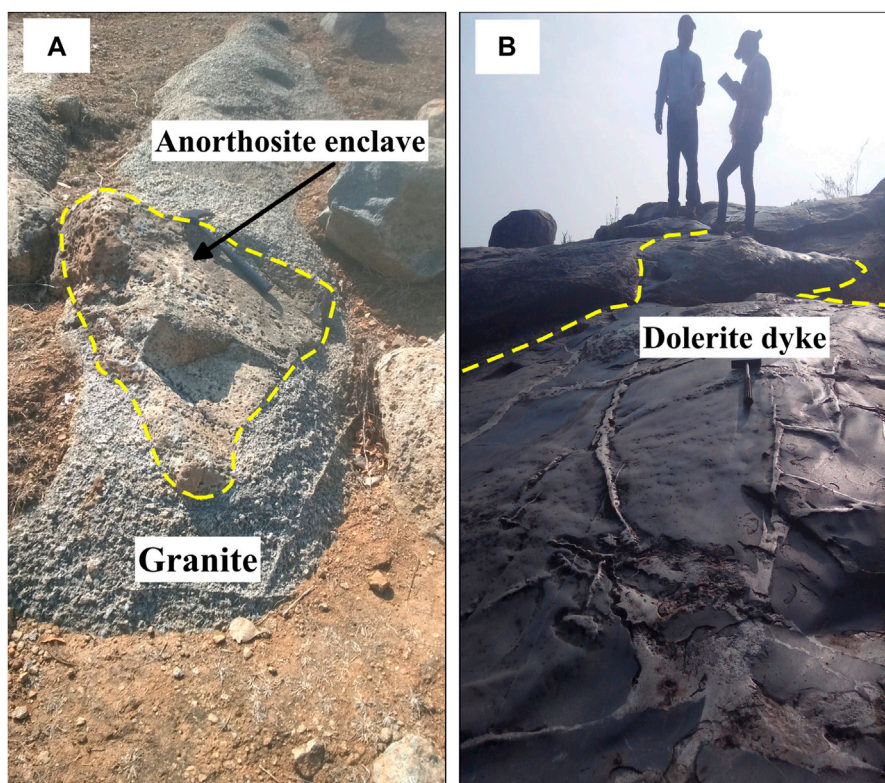


**FIGURE 4**

Field occurrence of (A) anorthosite enclave within granite (N 24°58'99", E 85°12'08.22") (B) dolerite dyke (N 24°58'35.7", E 85°12'08.22") cross-cutting the anorthosite enclave bearing granite pluton.

### 3 Analytical techniques

#### 3.1 Thin section

Thin sections were studied in a Nikon E-200 POL petrographic microscope using plane and cross-polarized transmitted light to identify locations suitable for *in-situ* assessment of mineral chemistry via electron-probe microanalyzer (EPMA) instrument, i.e., without surface scratches or mineral/fluid inclusions. Mineral names are abbreviated where appropriate following [Whitney and Evans \(2010\)](#). Modal contents were visually estimated in volume percent (vol%).

#### 3.2 Electron-probe analysis

Compositions of minerals were analyzed on CAMECA SX-5 EPMA at the DST-SERB National Facility, Department of Geology (Center of Advanced Study), Institute of Science,

Banaras Hindu University. The instrument was operated at an accelerating voltage of 15 kV and a beam current of 10 nA using a LaB<sub>6</sub> electron source. The positions of crystals (SP1-TAP, SP2-LiF, SP3-LPET, SP4-LTAP, and SP5-PET) and wavelength dispersive spectrometers were verified using andradite as an internal standard. The X-ray lines that were used for analyses include F-K $\alpha$ , Na-K $\alpha$ , Mg-K $\alpha$ , Al-K $\alpha$ , Si-K $\alpha$ , P-K $\alpha$ , Cl-K $\alpha$ , K-K $\alpha$ , Ca-K $\alpha$ , Ti-K $\alpha$ , Cr-K $\alpha$ , Mn-K $\alpha$ , Fe-K $\alpha$ , Ni-K $\alpha$ , and Ba-La. The routine calibration and quantification of data were performed with the help of natural mineral standards supplied by CAMECA-AMETEK, which include fluorite, halite, periclase, corundum, wollastonite, apatite, orthoclase, rutile, chromite, rhodonite, hematite, barite, and Ni pure metal. Routine calibration, acquisition, quantification, and data processing were performed with the help of SxSAB (version 6.1) and SX-Results software supplied by CAMECA. Analysis precision is better than 1% for major oxides and 5% for trace elements. Further details on the analytical procedure can be obtained from [Pandey et al. \(2019\)](#).

**TABLE 1** Whole-rock composition of the studied anorthosite samples from the Chotanagpur Granite Gneiss Complex via X-ray fluorescence spectrometer and inductively coupled plasma mass spectrometer.

Rock	Anorthosite		RJ 45B	RJ 48B	RJ 48C	RJ 40	RJ 48D	RJ 46	BR 19	BR 21
Sample	RJ 45A	RJ 45C								
<i>Major oxides (wt%)</i>										
SiO <sub>2</sub>	50.61	50.37	50.22	50.14	46.85	58.23	47.47	50.38	48.08	45.69
TiO <sub>2</sub>	0.39	0.27	0.31	0.36	0.53	1.17	0.55	0.88	0.34	0.43
Al <sub>2</sub> O <sub>3</sub>	23.88	25.12	25.03	24.01	17.87	15.98	25.81	12.75	24.36	18.15
Fe <sub>2</sub> O <sub>3</sub> (t)	6.41	4.83	5.46	5.66	12.5	8.46	6.13	10.23	4.02	8.89
MnO	0.07	0.05	0.05	0.05	0.17	0.06	0.07	0.17	0.06	0.12
MgO	3.1	2.74	2.63	2.78	6.44	2.82	2.59	8.42	4.08	9.25
CaO	12.38	12.93	11.88	12.05	11.25	4.03	14.51	10.74	16.13	13.96
Na <sub>2</sub> O	1.95	1.99	1.8	1.71	1.17	3.07	1.84	1.92	1.2	0.76
K <sub>2</sub> O	0.87	0.77	1.8	1.48	1.25	2.79	0.57	1.61	0.44	0.71
P <sub>2</sub> O <sub>5</sub>	0.1	0.11	0.07	0.2	0.37	0.77	0.08	0.27	0.05	0.02
LOI	1.65	1.2	1.63	1.52	1.47	0.61	1.71	1.97	1.7	2.52
Total	101.41	100.38	100.88	99.96	99.87	97.38	101.33	99.34	100.46	100.5
Mg#	48.92	52.90	48.82	49.30	50.50	39.76	45.55	61.97	66.77	67.32
<i>Trace element (ppm)</i>										
Ba	117	107	204	184	105	1,202	102	315	67	86
Cr	251	196	191	214	175	249	274	136	236	451
V	69	43	58	68	157	80	109	217	87	194
Sc	20	17	15	17	38	14	20	44	24	35
Co	13	9	10	10	42	11	12	46	12	41
Ni	13	10	9	11	58	24	22	58	20	45
Cu	17	10	37	34	77	26	48	71	21	7
Zn	51	40	53	59	125	98	45	93	33	67
Ga	24.85	24.76	24.32	23.67	23.19	29.21	24.64	17.96	20.25	18.15
Pb	7	5.9	8.5	7.3	4.5	20.2	6.1	11.7	5.2	8.8
Th	1.19	1.92	3.22	3.2	2.45	53.27	2.87	7.71	1	1.4
Rb	59	48	117	104	125	250	29	72	18	31
Sr	196	198	199	190	166	261	201	275	173	149
Y	12	9	19	17	31	40	9	29	6	11
Zr	33	21	28	32	19	587	33	98	9	13
Nb	5	4.3	3.8	4.3	4.2	53	4.7	9	3.1	1.9
U	BDL	BDL	1.75	BDL	BDL	2.52	BDL	BDL	0.7	0.4
La	7.60	6.11	1.60	11.62	0.82	181.20	8.00	3.40	8.38	6.12
Ce	15.49	11.73	13.82	22.50	7.53	350.00	16.59	8.43	15.58	11.86
Pr	1.58	1.15	0.39	2.70	0.19	40.23	1.76	0.81	1.99	1.53
Nd	5.85	4.01	1.40	9.84	0.80	138.00	6.31	2.92	6.83	5.84
Sm	1.14	0.72	0.23	1.98	0.13	22.63	1.20	0.58	1.36	1.32
Eu	0.75	0.66	0.06	0.89	0.05	3.48	0.66	0.11	0.79	0.58
Gd	1.19	0.71	0.27	1.99	0.16	20.62	1.19	0.57	1.49	1.43
Tb	0.18	0.10	0.03	0.31	0.02	2.35	0.18	0.09	0.21	0.22
Dy	1.11	0.62	0.17	1.82	0.11	9.85	1.03	0.57	1.19	1.35
Ho	0.23	0.13	0.03	0.37	0.02	1.53	0.21	0.13	0.23	0.29
Er	0.62	0.35	0.10	1.00	0.06	3.37	0.55	0.40	0.65	0.75
Tm	0.10	0.05	0.01	0.14	0.01	0.38	0.08	0.07	0.09	0.11
Yb	0.68	0.37	0.10	0.91	0.06	2.22	0.53	0.50	0.64	0.75

(Continued on following page)

TABLE 1 (Continued) Whole-rock composition of the studied anorthosite samples from the Chotanagpur Granite Gneiss Complex via X-ray fluorescence spectrometer and inductively coupled plasma mass spectrometer.

Rock	Anorthosite		RJ 45B	RJ 48B	RJ 48C	RJ 40	RJ 48D	RJ 46	BR 19	BR 21
Sample	RJ 45A	RJ 45C								
Lu	0.10	0.06	0.02	0.13	0.01	0.33	0.08	0.09	0.10	0.11
CIPW Norm (wt%)										
PLAG	78.76	82.46	82.89	81.11	58.68	74.39	80.13	48.93	74.53	56.19
CPX	7.85	6.70	4.71	6.39	15.46	5.62	11.50	29.52	17.86	23.29
OPX	13.39	10.84	12.40	12.50	19.38	17.61	4.46	17.74	7.61	6.56
OL	0.00	0.00	0.00	0.00	6.47	0.00	3.91	3.81	0.00	13.96

Note: BDL, below detection limit; PLAG, plagioclase; CPX, clinopyroxene; OPX, orthopyroxene, Ol, olivine.

### 3.3 Bulk rock major oxide and trace chemistry

The WR (major, trace, and rare earth element [REE] chemistry) analyses were conducted at the Wadia Institute of Himalayan Geology, Dehradun, India. Major oxides and selected trace elements were analyzed using an X-ray fluorescence spectrometer (XRF; Bruker S8 Tiger). The detailed sample digestion procedure was as follows. Sample powders (200 mesh) were dried in an oven at 105°C for 12 h. About 1.0 g of the dried powder was accurately weighed in a ceramic crucible and then heated in a muffle furnace at 1,000°C for 2 h. After cooling to 400°C, the samples were placed in the drying vessel and weighed again to calculate the loss on ignition. About 0.6 g sample powder was mixed with 6.0 g cosolvent and 0.3 g oxidant in a Pt crucible and heated in a furnace at 1,150°C for 14 min. Then, the sample was quenched in the air for 1 min to produce flat disks for the XRF analyses.

The REEs were analyzed using an inductively coupled plasma mass spectrometer (ICP-MS; Perkin Elmer SCIEX ELAN DRC-e). The procedures for sample digestion and preparation of solutions for ICP-MS analyses are after Balaram et al. (1990). The USGS (BHVO-1, AGV-1) and JGS (JG-2, RGM-1) rock standards were used to calibrate the ICP-MS and keep a check on data quality. The major, trace, and REE data of the anorthosite samples are given in Table 1, whereas those of diorite, hornblendite, pyroxenite, granite, and dolerite samples are listed in Table 2. Overall accuracy and precision (RSD) are <5% and 2–3% for major/minor oxides and <12% and 10% for trace elements, respectively (Purohit et al., 2006; Saini et al., 2007).

### 3.4 Mineral trace element and rare earth element chemistry

Trace element concentrations in plagioclase were measured *in-situ* in thin sections using a Thermo Fisher

Scientific iCAP-Q ICP-MS coupled with a New Wave Research 193 ArF Excimer laser ablation system at the Radiogenic Isotope Facility, Department of Geology and Geophysics, IIT Kharagpur. The analyses were conducted at a spot size of 50 μm, a laser repetition rate of 10 Hz, and a fluence of 6 J/cm<sup>2</sup>. The ICP-MS was optimized for maximum sensitivity on Li, Co, In, Th, and U while keeping the oxide production rate below 0.8–1.0%. External standardization was conducted by bracketing 10 measurements of the samples by two analyses of NIST 610 reference glass. The data quality was monitored by ablating the NIST 612 and NIST 610 reference glasses as unknowns together with the samples. The accuracy and precision are better than 10% for most trace elements. The trace element data from multiple analyses of the NIST 612 and NIST 610 reference glasses are provided in Supplementary Table S1.

## 4 Results

### 4.1 Petrography and mineral chemistry

#### 4.1.1 Host granite

Granite is the host lithology of this terrain. It is coarse-grained, leucocratic, and massive. It is composed of quartz, feldspar (plagioclase and K-feldspar), and biotite. The granite modally consists of K-feldspar (35–40 wt%), quartz (30–35 wt%), plagioclase (20–30 wt%), biotite (5–10 wt%), and accessory phases (<1 wt%) and displays equigranular texture (Figures 5A, B).

The chemical compositions of feldspar, biotite, epidote, and iron oxide quantified via EPMA in the studied granites are listed in Supplementary Tables S2A–E. Plagioclase composition ranges from oligoclase to andesine (An<sub>15–31</sub>), whereas the K-feldspar is orthoclase (Or<sub>90–100</sub>) (Supplementary Figure S1). Biotite is phlogopite and Mg-biotite (Supplementary Figure S2). The Fe-oxide is mostly magnetite. Epidote occurs as an accessory phase in the host granite.

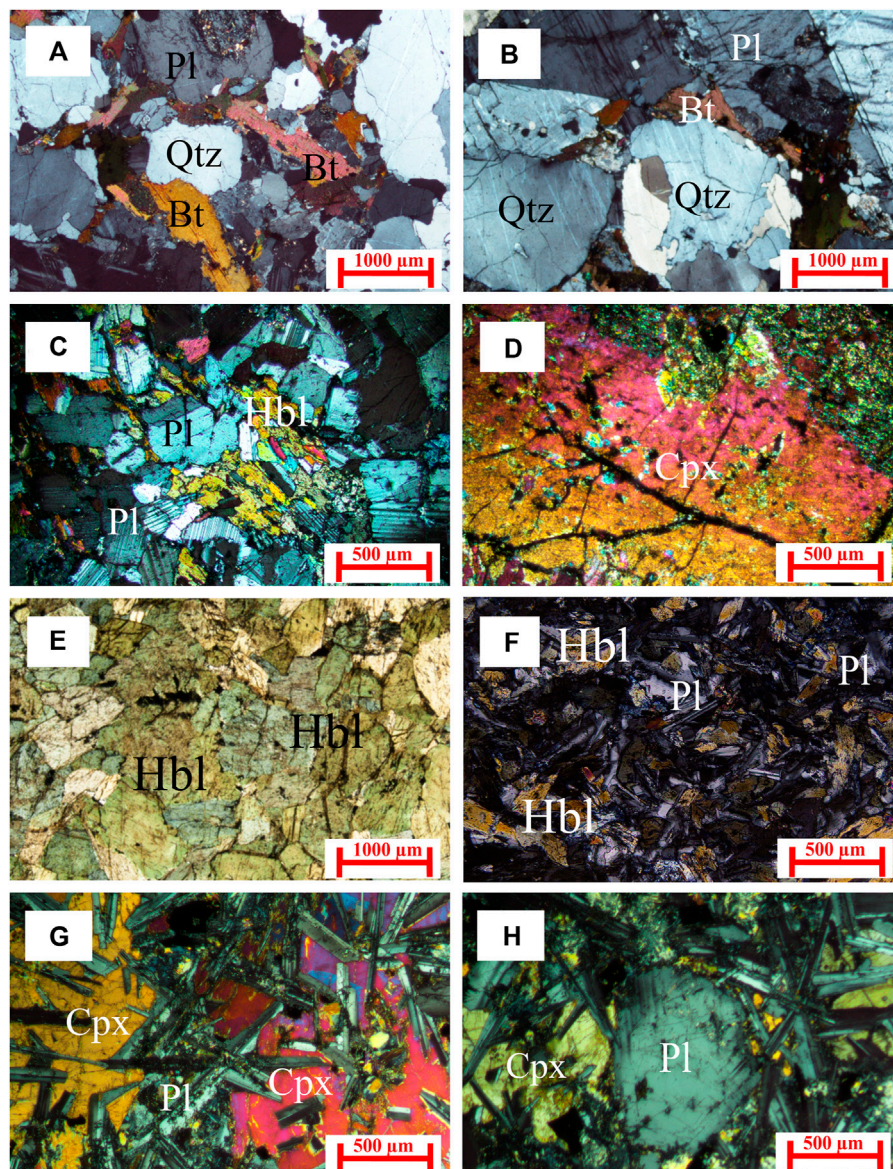


**FIGURE 5**

Photomicrograph of (A,B) granite host rock showing association of quartz, biotite, and feldspars. (C) anorthosite showing cumulate grains of anorthite with intercumulus hornblende, (D) pyroxenite with phenocryst of clinopyroxene, (E) hornblende showing cumulate texture with a hornblende volume percentage of ~80–90%, (F) typical assemblage of plagioclase and hornblende and biotite in diorite. (G,H) dolerite with the typical assemblage of pyroxene and plagioclase showing ophitic to subophitic texture.

## 4.1.2 Enclaves

### 4.1.2.1 Anorthosite

Anorthosites comprise an assemblage of well-formed feldspar macrocrysts interspersed with a fine-grained interstitial mass of fine-grained amphibole and biotite. A minor amount of iron oxide is also observed. Biotite and amphibole are late phases formed from the intercumulus melt. Plagioclase feldspar mostly occurs as randomly

oriented tabular subhedral to euhedral laths (Figure 5C). A minor amount of hornblende and biotite occur as clots within the intergranular spaces between the tabular plagioclase crystals.

The chemical compositions of feldspar, amphibole, biotite, chlorite, and epidote in the anorthosites quantified via EPMA are listed in Supplementary Tables S3A–D. The plagioclase composition ranges from  $An_{87-94}$ , and these are classified as

bytownite and anorthite (Supplementary Figure S1). Biotite is Mg-biotites and phlogopite (Supplementary Figure S2). The amphibole is classified as magnesiohornblende and ferrotschermakite (Supplementary Figure S3) with high Si (6.10–7.13 a.p.f.u) and  $X_{Mg}$  [ $Mg/(Mg + Fe^{2+})$ ] varying between 0.40 and 0.62 suggestive of an igneous origin (Sial et al., 1998). Fe-chlorite (Type 1; Zane and Weiss, 1998) is a secondary phase formed by the alteration of pyroxene and amphibole. Epidote is an accessory phase in anorthosite.

#### 4.1.2.2 Pyroxenite

The pyroxenites are coarse-grained with an average grain size of 4–5 mm. They contain clinopyroxene (>90 vol%) and amphibole with minor ilmenite-magnetite. Clinopyroxene occurs as a subhedral to anhedral coarse-grained cumulate phase (Figure 5D). Chlorite is the common altered product of clinopyroxene. Hornblende grains are present as anhedral, medium- to coarse-grained cumulate phases. They occupy the spaces between the cumulates. The studied pyroxenite rocks show adcumulate texture, wherein clinopyroxene and amphibole occur as cumulates and Fe–Ti oxides as the intercumulus phases.

The chemical compositions of clinopyroxene, amphibole, and iron oxides quantified via EPMA in the studied pyroxenites are listed in Supplementary Tables S4A–C. Clinopyroxene is of diopside and augite composition (Supplementary Figure S4), with a compositional range of  $Wo_{29-50} Fn_{39-52} Fs_{10-19}$ . The studied amphibole of pyroxenite enclaves is classified as magnesiohornblende and actinolite (Supplementary Figure S3). Actinolite seems to be an alteration product. The Fe-oxides observed in the pyroxenite are ilmenite and magnetite.

#### 4.1.2.3 Hornblendite

The hornblendite sample (Figure 5E) is mainly composed of medium- to fine-grained idiomorphic and equigranular hornblende (cumulus hornblende ranges from 1 to 2 mm, and intercumulus clinopyroxene crystals are <600  $\mu m$ ), occasionally skeletal, with minor inclusions of exsolved Fe–Ti oxides and interstitial anorthositic plagioclase (<600  $\mu m$ ). Amphibole crystals are randomly oriented, and grain boundaries are commonly smooth, curvilinear, and sutured. Euhedral hornblende displays orthocumulate texture with intercumulus plagioclase, suggesting high-temperature crystallization for the amphibole before plagioclase. Neither reaction textures nor relicts are observed in this rock. Accessory phases are disseminated granular magnetite–ilmenite pairs that occur on the interfaces of clinopyroxene and amphibole.

The chemical compositions of amphiboles, plagioclases, clinopyroxenes, biotites, chlorites, iron oxides, and apatite quantified via EPMA in the studied hornblendite are listed in

Supplementary Tables S5A–G. The amphiboles are classified as magnesiohornblende and actinolite (Supplementary Figure S3). Magnesiohornblendes are primarily igneous, and actinolite seems to be of alteration product of clinopyroxenes. The plagioclase composition range from  $An_{8-82}$  (albite and bytownite) (Supplementary Figure S1). Albite could be the low-temperature alteration product. The clinopyroxene composition of the hornblendite varies from  $En_{43-53} Wo_{27-30} Fs_{19-26}$  (Supplementary Figure S3). Biotite is phlogopite and Mg-biotite based on classification after Rieder et al. (1998) (Supplementary Figure S2). Type I trioctahedral Fe-chlorites are present as a secondary mineral formed by the alteration of amphibole and pyroxene. The Fe–Ti oxide phase is mostly ilmenite. Apatite is present as an accessory phase in the hornblendite.

#### 4.1.2.4 Diorite

The modal composition of diorite includes plagioclase (~75–80 vol%), amphibole (~15–20 vol%) quartz (~3 vol%), and iron oxide (~1 vol%) (Figure 5F). Plagioclase occurs as subhedral tabular crystals displaying lamellar twinning. It is unzoned and partly replaced by white mica. Hornblende is abundant and partially chloritized. The opaque minerals are represented by homogeneous subhedral ilmenite grains.

The chemical compositions of plagioclase, amphibole, and a minor amount of chlorite quantified via EPMA in the studied diorite are listed in Supplementary Tables S6A–C. The amphibole is classified as magnesiohornblende and ferrotschermakite to actinolite with Si (6.35–7.96 a.p.f.u.) and  $X_{Mg}$  (0.48–0.83) showing a large variation. Chlorite in the diorites is Fe-chlorite (after Zane and Weiss, 1998).

#### 4.1.3 Syn-plutonic mafic dyke

The dolerites are medium- to fine-grained porphyritic varieties. Euhedral plagioclase is the dominant phenocryst phase, commonly 100–300  $\mu m$  across. The groundmass comprises subhedral plagioclase, clinopyroxene, and trace Fe–Ti oxides. Minor plagioclase and clinopyroxene grains in the samples are partially altered to epidote and amphibole. Plagioclase is fully or partially engulfed by clinopyroxene resulting in subophitic and ophitic texture (Figures 5G, H).

The chemical compositions of clinopyroxene, plagioclases, amphibole, and iron oxide quantified via EPMA in the dolerite are listed in Supplementary Tables S7A–D. The plagioclase ranges from albite to bytownite ( $An_{1-73}$ ) (Supplementary Figure S1). Clinopyroxene from the dolerite is mainly diopside to augite with the compositional range  $Wo_{26.72-43.93} En_{35.38-40.95} Fs_{18.78-33.76}$  (Supplementary Figure S4). The iron oxides in dolerite are mainly ilmenite. The studied amphiboles in dolerite are classified as

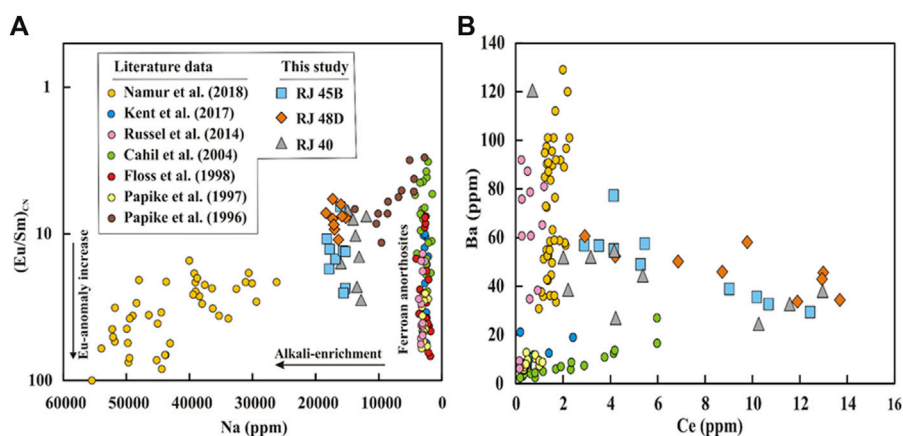


FIGURE 6

(A)  $(Eu/Sm)_{CN}$  vs. Na (ppm) (after Joy, 2013; Russell et al., 2014) and (B) Ba (ppm) vs. Ce (ppm) plots for plagioclase. For Namur and Humphreys (2018), Sr >950 ( $n = 3$ ) and Ba >240 ( $n = 1$ ) were not considered in the plot. Normalizing values are taken from Sun and McDonough (1989).

ferroactinolite to actinolite with Si (7.59–7.78 a.p.f.u.) and the  $X_{Mg}$  [ $Mg/(Mg + Fe^{2+})$ ] varying from 0.5 to 0.7. They are of igneous origin as seen in the Si vs. Na + Ca + K plot (Sial et al., 1998).

## 4.2 Trace element and rare earth element of plagioclase in anorthosite

Trace element data (in ppm) of representative plagioclase from anorthosite samples RJ 48D, RJ 45B, and RJ 40 were obtained and are listed in Supplementary Table S1. The abundance of large ion lithophile elements (LILE; e.g., Cs, Rb, K, Ba, Sr, and Eu) and high field strength elements (HFSE; e.g., Ti, Zr, Nb, U, Th, and Ce) are quite consistent across the three samples as displayed in Supplementary Figure S5. Among the HFSE, elements such as Zr, Nb, Th, and U are seen to be constrained between rock/chondrite = 0.01–0.1.

Trace elements in plagioclase have been widely used to distinguish magmatic rocks, particularly lunar rocks. In the  $(Eu/Sm)_{CN}$  (degree of Eu anomaly) vs. Na (proxy for plagioclase An) plot (after Joy, 2013; Russell et al., 2014), the ferroan lunar anorthosites (Papike et al., 1997; Floss et al., 1998; Cahill et al., 2004; Russell et al., 2014; Kent et al., 2017) trend vertically on the extreme right between Na = 1,504–4,246 ppm (Figure 6A). The plagioclase of this study is constrained between Na = 11,961–29,267 ppm, whereas the plagioclase of Skaergaard Intrusion, Greenland (Namur and Humphreys, 2018), displays broad variations from Na = 26,200–55,462 ppm. The lunar plagioclase of Papike et al. (1996) shows a transition between ferroan anorthosites and samples of this study. In the Ba (ppm) vs. Ce (ppm) plot, the plagioclase of this study displays an increasing Ce trend, which is most likely because of fractional

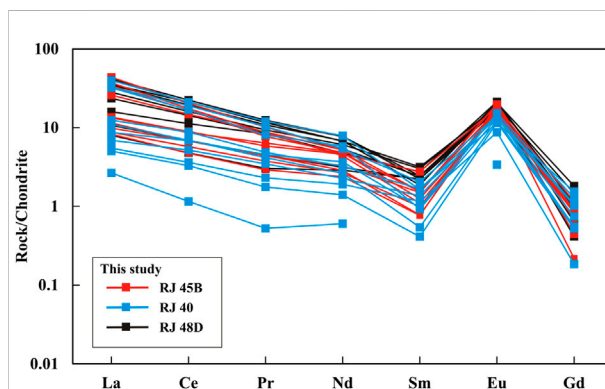


FIGURE 7

Chondrite normalized rare earth element patterns for plagioclase in anorthosite samples RJ 45B, RJ 40, and RJ 48D from the Chotanagpur Granite Gneiss Complex. Normalizing values are taken from Sun and McDonough (1989).

crystallization (Figure 6B). The plagioclase of lunar rocks and Skaergaard Intrusion, Greenland, conversely, show an increasing Ba trend, which is likely generated by progressive melting of the source or mixing of two magmas from different sources (e.g., Nielsen et al., 2020).

In the chondrite (C1; Sun and McDonough, 1989) normalized diagram (Figure 7), REEs (La to Gd) of analyzed plagioclase in the three samples display similar enrichment and overall increasing trend from Gd (plagioclase/C1 = ~0.18–1.81) to La (plagioclase/C1 = ~2.66–43.67) but with a strong positive Eu anomaly. HREEs are not shown because of a lack of sensitivity because of low contents in plagioclase. Plagioclase analysis of sample RJ 40 displays relatively low REE enrichment.

TABLE 2 Whole-rock composition of the studied diorite, hornblende, pyroxenite, granite, and dolerite samples from the Chotanagpur Granite Gneiss Complex via X-ray fluorescence spectrometer and inductively coupled plasma mass spectrometer.

Rock	Diorite	Hornblende		Pyroxenite	Granite	BR 4	Dolerite	BR 17	BR 20	BR 22
Sample	BR 9/1	BR 18	BR 9/3	BR 9/4	BR 1		BR 9/5			
<i>Major oxides (wt%)</i>										
SiO <sub>2</sub>	49.92	45.95	47.87	47.75	71.58	68.93	45.39	45.45	45.1	45.24
TiO <sub>2</sub>	0.91	0.47	0.48	0.69	0.33	0.26	2	2.21	2.2	2.2
Al <sub>2</sub> O <sub>3</sub>	14.71	8.04	3.97	3.75	13.83	15.79	12.65	14.25	13.91	14.1
Fe <sub>2</sub> O <sub>3</sub> (t)	11.74	16.4	16.11	16.37	3.52	3.46	14.67	15.1	15.08	14.93
MnO	0.18	0.26	0.26	0.28	0.06	0.07	0.22	0.2	0.2	0.2
MgO	7.04	17.63	14.69	16.8	0.15	0.67	8.38	7.77	7.55	7.42
CaO	9.26	6.19	12.92	11.4	1.27	2.02	10.16	9.52	9.97	9.71
Na <sub>2</sub> O	1.7	0.28	0.52	0.2	3.32	3.4	1.96	2.01	1.81	1.96
K <sub>2</sub> O	1.04	0.17	0.32	0.07	5.34	4.89	0.76	0.87	0.54	0.69
P <sub>2</sub> O <sub>5</sub>	0.22	0.02	0.01	0.03	0.03	0.11	0.24	0.26	0.27	0.27
LOI	3.49	5.71	1.09	2.56	1.24	1.31	3.59	2.37	2.62	2.51
Total	100.21	101.12	98.24	99.9	100.67	100.91	100.02	100.01	99.25	99.23
Mg#	54.28	68.04	64.36	67.02	7.78	27.72	53.08	50.47	49.78	49.60
<i>Trace element (ppm)</i>										
Ba	327	60	19	22	881	398	219	245	194	207
Cr	158	440	483	476	71	106	256	193	195	246
V	208	256	455	451	8	22	306	302	316	311
Sc	27	43	91	80	7.9	7.9	36	33	35	33
Co	39	98	106	121	17.1	40.1	57	52	51	53
Ni	57	157	193	234	12	9	85	79	75	76
Cu	31	81	26	28	13	6	55	50	55	52
Zn	103	107	82	87	66	58	94	116	124	100
Ga	20.24	13.02	6.91	7	18	18	18.58	20.69	19.87	19.46
Pb	5.8	BDL	1.7	7.5	23	34	4.7	1.7	4.5	2.8
Th	16.04	4.16	1.32	BDL	25	29	2.85	0.8	0.5	0.8
Rb	27	4	2	2	238	266	25	32	22	29
Sr	205	19	18	15	64	97	264	271	261	263
Y	23	13	14	13	55	37	28	31	29	31
Zr	105	23	17	12	241	117	114	115	117	121
Nb	8	3.8	2.3	BDL	21	21	9.3	9.1	10.5	8.4
U	<1.0	<1.0	<1.0	<1.0	BDL	BDL	BDL	BDL	BDL	BDL
La	10.66	2.82	0.36	1.62	43.73	28.68	7.05	10.25	5.62	9.9
Ce	35.41	7.53	1.36	4.87	93.31	66.31	18.55	25.17	19.95	24.05
Pr	3.62	1.00	0.17	0.86	11.05	7.54	2.66	3.71	2	3.58
Nd	14.24	4.12	0.69	4.25	41.23	27.68	12.04	17.01	9.05	16.26
Sm	3.00	0.97	0.23	1.45	8.47	5.87	2.99	4.27	2.11	4.05
Eu	0.71	0.31	0.06	0.27	1.43	0.58	1.12	1.73	0.8	1.64
Gd	2.94	1.06	0.26	1.70	8.89	5.32	3.15	4.66	2.36	4.36
Tb	0.40	0.19	0.04	0.30	1.38	0.72	0.49	0.76	0.35	0.7
Dy	2.05	1.11	0.25	1.94	8.24	3.66	2.88	4.58	2.04	4.16
Ho	0.40	0.25	0.06	0.41	1.74	0.70	0.59	0.96	0.42	0.86
Er	1.05	0.69	0.12	1.05	4.70	1.77	1.48	2.42	1.08	2.21
Tm	0.15	0.11	0.02	0.15	0.72	0.26	0.21	0.36	0.15	0.32
Yb	0.99	0.76	0.08	0.95	4.57	1.57	1.32	2.31	1.03	2.08
Lu	0.15	0.11	0.01	0.13	0.67	0.24	0.19	0.34	0.16	0.31

Note: BDL, below the detection limit.

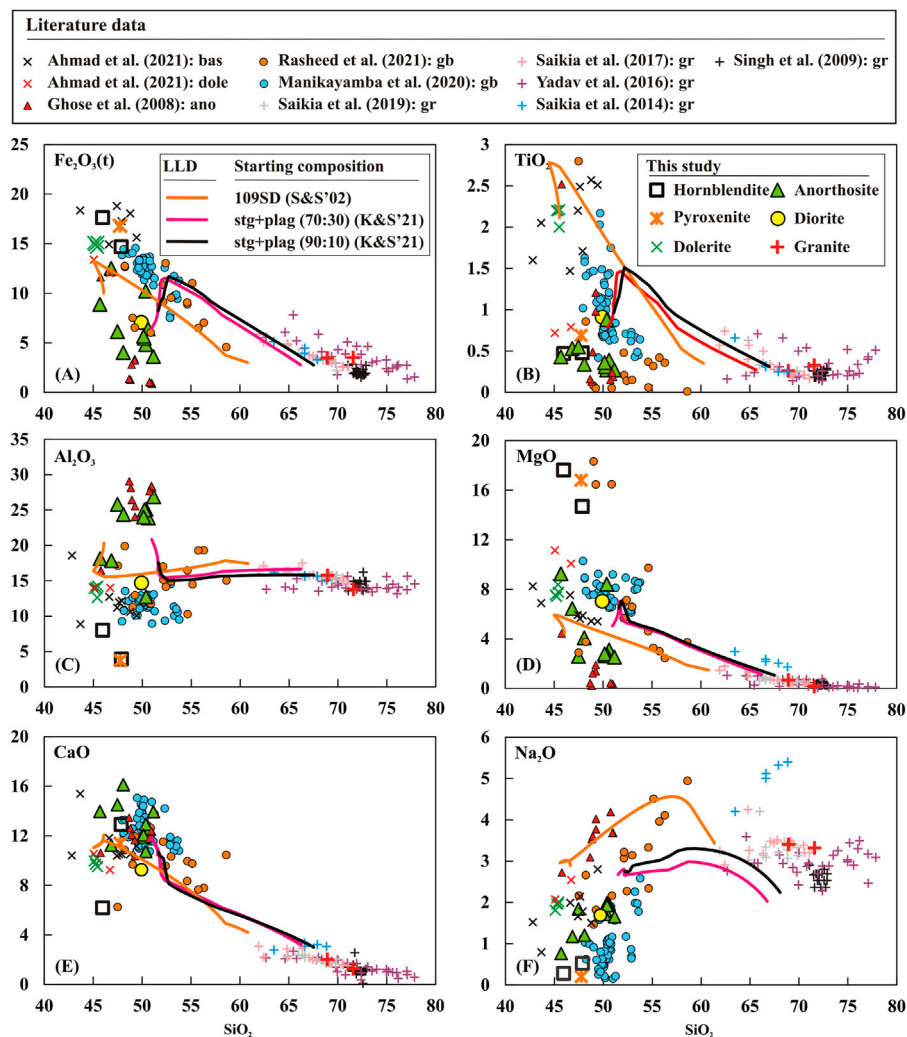


**FIGURE 8**

(A–F) major oxides vs.  $\text{SiO}_2$  plots. Lines represent the liquid line of descent calculated using MELTS (Gualda et al., 2012) at  $p = 3$  kbar,  $\text{H}_2\text{O} = 1$  wt %, and oxygen buffer = QFM. Rock abbreviations are from Chace (1956): bas, basalt; dole, dolerite; ano, anorthosite; dio, diorite; and gr, granite. S&S'02- Selbekk and Skjertie (2002); K&S'21- Krättili and Schmidt (2021).

### 4.3 Whole-rock geochemistry

Representative WR major and trace element compositions of the anorthosite, diorite, hornblende, and pyroxenite are given in Table 2. A plot of selected major oxides vs.  $\text{SiO}_2$  content is shown in Figures 8A–F, and selected trace elements vs.  $\text{SiO}_2$  content are shown in Supplementary Figures S6A–F. Literature data of selected plutonic rocks from CGGC are also plotted to figure out the overall geochemical trends in the region. In the anorthosite rocks (Ghose et al., 2008; this study), both  $\text{Fe}_2\text{O}_3(\text{T})$  and  $\text{MgO}$  contents decline steeply, whereas  $\text{Al}_2\text{O}_3$  increases sharply with an increase in  $\text{SiO}_2$  from 45.69 to 51.16 wt%. In the gabbro (Manikayamba et al., 2020; Rasheed et al., 2021) and granite (Singh and Krishna,

2009; Saikia et al., 2014; Yadav et al., 2016; Saikia et al., 2017; Saikia et al., 2019) rocks, both  $\text{Fe}_2\text{O}_3(\text{T})$  and  $\text{MgO}$  decrease gradually with increase in  $\text{SiO}_2$  from ~48 to ~78 wt%.

In the selected trace elements vs.  $\text{SiO}_2$  plots (Supplementary Figure S6), most trace elements of CGGC rocks appear to form two clusters, with  $\text{SiO}_2 = \sim 60$  wt% forming the dividing line. Hornblende, pyroxenite, basalt, dolerite, gabbro, and anorthosite rocks of CGGC cluster at  $\text{SiO}_2 < \sim 60$  wt%, whereas granites cluster at  $\text{SiO}_2 > \sim 60$  wt%. Rocks with  $\text{SiO}_2 < \sim 60$  wt% are relatively more enriched in Ni, Sc, V, and Sr but depleted in Pb and Th than rocks with  $\text{SiO}_2 > \sim 60$  wt% (Supplementary Figure S6). To test whether the two groups of rocks are genetically related, we made incompatible trace element ratio plots of Nb/Th vs. Zr/Sm and Sr/Y vs. La/

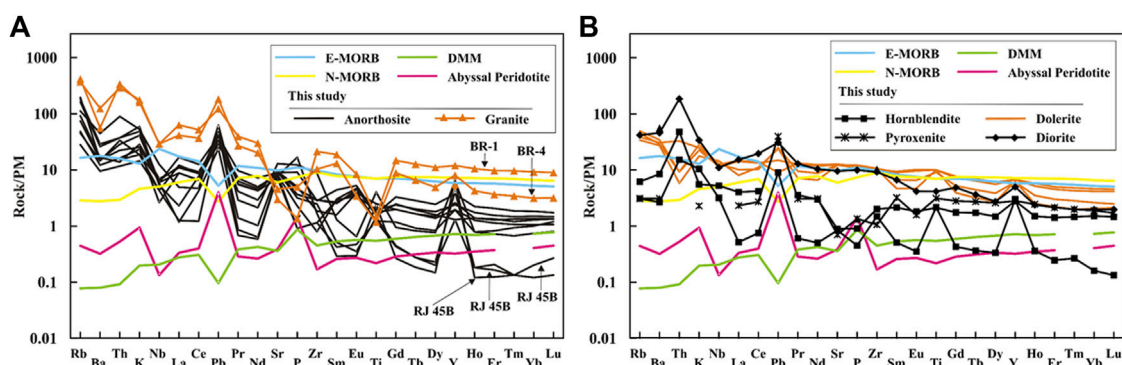


FIGURE 9

PM normalized whole-rock trace element patterns for (A) anorthosite and granite samples and (B) hornblende, pyroxenite, dolerite, and diorite samples from the Chotanagpur Granite Gneiss Complex (references as in Figure 7). Average enriched-MORB and normal-MORB from Sun and McDonough (1989), depleted MORB mantle from Workman and Hart (2005), and abyssal peridotite from Niu (2004). Normalizing values are taken from Sun and McDonough (1989).

Yb (Supplementary Figures S7A, B), since incompatible trace element ratios do not change significantly during <50% fractional crystallization. It is seen that the two groups of CGGC rocks do not display a single trend, and therefore, it is likely that they do not have a cogenetic source.

In this study, the PM (Sun and McDonough, 1989) normalized trace element patterns are shown in Figure 9A for anorthosite and granite samples and in Figure 9B for pyroxenite, hornblende, diorite, and dolerite samples. The average trends for E-MORB and N-MORB (Sun and McDonough, 1989), DMM (Workman and Hart, 2005), and abyssal peridotite (Niu, 2004) are also shown for comparison. The anorthosite samples in Figure 9A display near-parallel enrichment trends that increase from right to left, with moderate to strong positive anomalies at Y, Ti, Sr, and Pb. However, anorthosite samples RJ 45B, RJ 48C, and RJ 40 are relatively less enriched with rock/PM < 1 for most elements from Lu to Sm. Normalized values of relatively more mobile elements such as Rb, Ba, Th, and K show less scattering, which suggests that anorthosite samples are relatively fresh and geochemical data are suitable for interpretation. Granite samples (BR-1 and BR-4) are slightly more enriched than the anorthosite and display moderate to strong negative anomalies at Ti, P, Sr, Nb, and Ba and a moderate positive anomaly at Pb. However, sample BR-4 is relatively less enriched than BR-1 in elements from Lu to Gd and displays a weak positive anomaly at Y.

Pyroxenite, hornblende, diorite, and dolerite samples of this study display near-parallel enrichment trends that slightly increase from right to left. However, anomalies differ between these rock types. Hornblende samples show weak to moderate positive spikes at Y, Ti, Pb, and Th. The pyroxenite sample shows a moderate positive anomaly at

Pb. Dolerite samples, in general, possess weak to moderate positive anomalies at Y and Ti and a moderate negative anomaly at Th. Moreover, dolerite shows an enrichment trend quite similar to E-MORB. The relative degree of enrichment among various rock types shown in Figure 9B is dolerite > gabbro > pyroxenite > hornblende.

The chondrite (Sun and McDonough, 1989) normalized REE patterns are displayed in Figure 10A for anorthosite and granite samples and in Figure 10B for pyroxenite, hornblende, diorite, and dolerite. The fields for gabbro and granite rocks of CGGC from previous studies are also shown for comparison, including average trends for E-MORB, N-MORB, DMM, and abyssal peridotite. Anorthosite samples, on the whole, display a very gradual and steady increase in REE enrichment from Lu to La [(La/Yb)<sub>N</sub> = 1.22–13.08] with near-parallel trends. Most of the anorthosite samples show weak to moderate positive Eu anomaly. However, samples RJ 45B and RJ 46 display weak negative Eu anomaly. Moreover, samples RJ 45B and RJ 48C show a slight spike at Ce. Also, Lu to Dy values in anorthite samples RJ 45B, RJ 40, and RJ 48C are more depleted than both DMM and average abyssal peridotite. Granite samples (BR-1 and BR 4) trend near parallel to anorthosite but are more enriched than the latter and show moderate negative anomaly at Eu.

In Figure 10B, chondrite normalized REE patterns for hornblende, pyroxenite, dolerite, and diorite samples display a variable degree of enrichment from rock/chondrite = ~1 (hornblende sample BR 9/3) to rock/chondrite = ~50 (dolerite samples). The overall enrichment pattern shows a slight increase from Lu to La. Hornblende sample BR 9/3, however, shows a lower enrichment trend at rock/chondrite = ~1. Pyroxenite and diorite samples display a weak negative Eu anomaly. The relative degree of REE enrichment among these

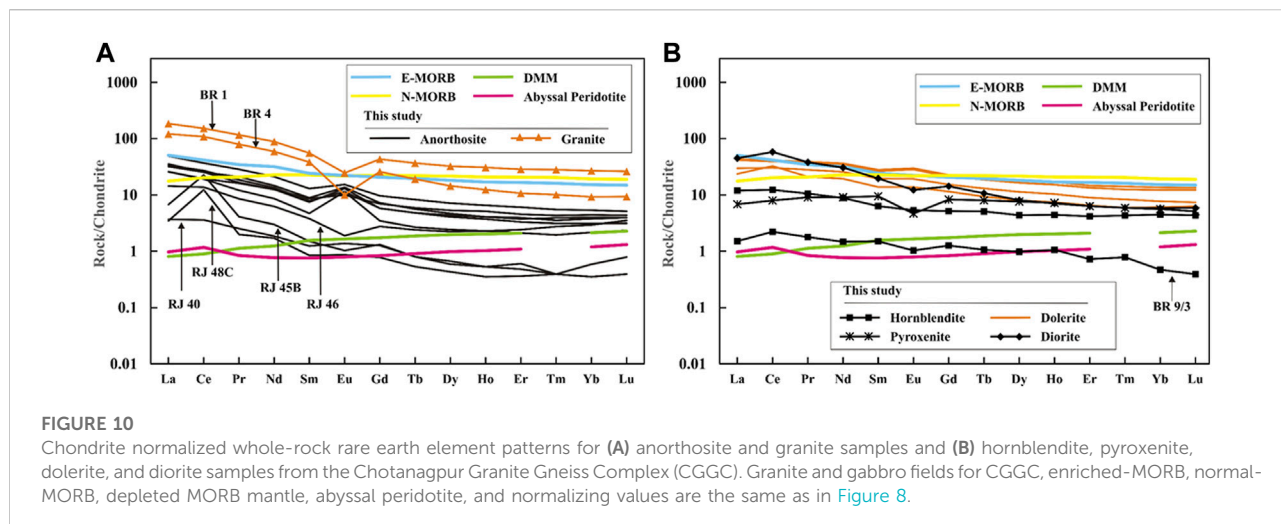


**FIGURE 10** Chondrite normalized whole-rock rare earth element patterns for (A) anorthosite and granite samples and (B) hornblende, pyroxenite, dolerite, and diorite samples from the Chotanagpur Granite Gneiss Complex (CGGC). Granite and gabbro fields for CGGC, enriched-MORB, normal-MORB, depleted MORB mantle, abyssal peridotite, and normalizing values are the same as in Figure 8.

**TABLE 3** Pressure and temperature of amphibole crystallization in pyroxenite, hornblende, and anorthosite samples from the study area.

Rock	Sample	P (kbar)					T (°C)	
		(a)	(b)	(c)	(d)	(e)	(f)	(g)
		(±1.4)	(±1.4)	(±0.9)		$\sigma_{est}$ 13.1%	(±30)	(±28)
Pyroxenite	BR 9/4	1.9–5.7 (n = 5)	1.4–5.0 (n = 5)	1.5–6.3 (n = 6)	0.2–1.0 (n = 9)	0.3–1.4 (n = 9)	635–800 (n = 9)	655–807 (n = 9)
Hornblende	BR 18, BR 9/3	2.0–6.6 (n = 13)	1.5–5.8 (n = 13)	2.3–5.1 (n = 12)	0.2–1.1 (n = 27)	0.3–1.9 (n = 27)	658–777 (n = 27)	672–788 (n = 27)
Anorthosite	RJ 45C	3.8–6.4 (n = 4)	3.2–5.7 (n = 4)	Mg# < 74	0.5–3.6 (n = 8)	0.5–3.4 (n = 8)	653–780 (n = 8)	669–775 (n = 8)

- (a) Larocque and Canil (2010).
- (b) Recalibrated Larocque and Canil (2010) (Krawczynski et al., 2012) (eq. 2).
- (c) Krawczynski et al. (2012), eq. 1) with  $\Delta NNO = 0$  and  $74 < Mg\# < 84$ .
- (d) Ridolfi et al. (2010).
- (e) Ridolfi and Renzulli (2012); eq. 1b).
- (f) Putirka (2016) (eq. 5) for P-independent.
- (g) Putirka (2016) (eq. 6) for P-dependent.

rock types shown in Figure 10B is dolerite > diorite > pyroxenite > hornblende.

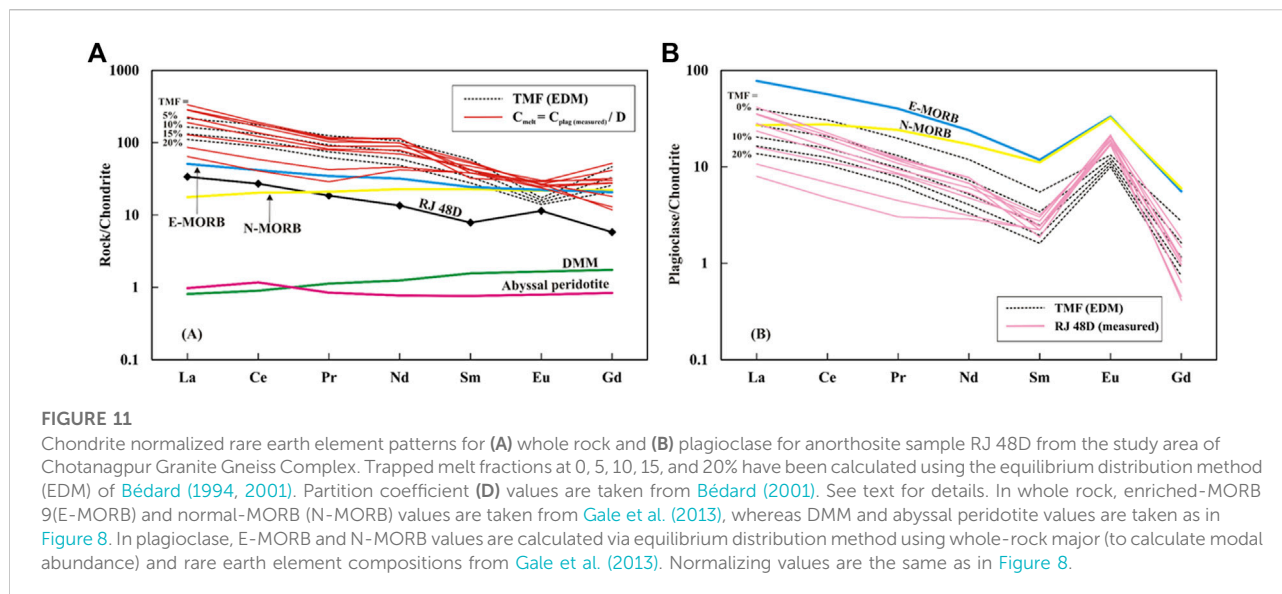
## 5 Discussion

### 5.1 Pressure and temperature of amphibole crystallization

In this study, pressure (P) and temperature (T) of amphibole crystallization were constrained using amphibole present in pyroxenite, hornblende, and anorthosite samples. P was calculated using the following barometers: 1) Larocque and Canil (2010) that uses  $Al^{VI}$  values in amphibole; 2) recalibrated Larocque and Canil (2010) barometer with added experiments of Krawczynski et al. (2012) (eq. 2); 3) barometer-

hygrometer of Krawczynski et al. (2012) (eq. 1) that uses Mg# (between 74 and 84) of the amphibole and assuming  $\Delta NNO = 0$ ; 4) Ridolfi et al. (2010); and 5) Ridolfi and Renzulli (2012) (eq. 1b). It was seen that barometers of Larocque and Canil (2010) and Krawczynski et al. (2012) (eq. 2) returned lower p values when  $Al^{VI} < 0.1$  a.p.f.u., but higher p values when  $Al^{VI} > 0.4$  a.p.f.u. in our samples and therefore were not considered. Also, only those p values of Krawczynski et al. (2012) (eq. 1) barometer were considered where Mg# of amphibole lie between 74 and 84. T was calculated using amphibole thermometers of Putirka (2016) (eq. 5 for P-independent and eq. 6 for P-dependent).

P-T values obtained using amphibole geothermobarometers are presented in Table 3. Pressure and temperature of amphibole crystallization are constrained between 0.2 and 6.3 kbar and 635–807°C for pyroxenite, 0.2–6.6 kbar and 658–788°C for hornblende, and 0.5–6.4 kbar and 653–780°C for anorthosite.



## 5.2 Parental melt calculation for anorthosite

The compositions of parental liquid for anorthosite from the study area were estimated by adopting the equilibrium distribution method (EDM; Bédard, 1994; Bédard, 2001). Input variables for EDM include WR composition of anorthosite, mineral proportions, mineral/melt partition coefficients, and trapped melt fractions (TMF). WR composition and mineral proportions (CIPW norm) are given in Table 1. Mineral/melt partition coefficients were taken from Bédard (2001), where they have been applied for an anorthosite suite of rocks. We selected anorthosite sample RJ 48D for EDM calculations because of the high modal abundance of plagioclase, presence of modal olivine, and availability of plagioclase trace element data. Parental melts were calculated assuming TMF between 0% and 20%, and the results are displayed in Figures 11A, B. Also shown are the average trends for N-MORB and E-MORB, DMM, and abyssal peridotite.

REE enrichment patterns from La to Gd at TMF between 0% and 20% are shown in Figure 11A for WR and in Figure 11B for plagioclase composition. WR melt curves in Figure 11A display a near-parallel and increasing trend from La to Gd with a negative anomaly at Eu. The melt curves trend near parallel to E-MORB but at slightly higher rock/chondrite values. Parental melt curves calculated using the Nernst distribution coefficient equation  $C_{melt} = C_{plag}/D_{plag}$  (where  $C_{melt}$  = concentration in melt,  $C_{plag}$  = concentration in plagioclase, and  $D_{plag}$  = plagioclase-melt partition coefficient) are also displayed in Figure 11A. It is seen that parental melt curves from Sm to La are near parallel and constrained broadly between TMF = ~5–15%, except for two lines that plot below TMF = 20%. WR sample RJ 48D in

general lies below N-MORB and E-MORB but above DMM and abyssal peridotite.

The plagioclase REE composition from Gd to La analyzed in sample RJ 48D is shown in Figure 11B. It is interesting to note that the degree and pattern of REE enrichment in plagioclase very closely resemble the TMF curves calculated via EDM using WR composition. The plagioclase compositions are near parallel to E-MORB with a strong positive anomaly at Eu. Also, plagioclase compositions from Sm to La are constrained between TMF = ~5–15%, which is similar to that observed in Figure 11A.

## 5.3 Petrogenesis of anorthosite

The origin of anorthosite has been a topic of discussion for more than 6 decades. Most of the earlier workers believed that anorthosite formation occurred through the crystallization of plagioclasic magma, which resulted from the assimilation of sedimentary rocks by basaltic magma (e.g., Waard et al., 1974, and references therein). It was thought that mantle-derived magmas ponded at the crust–mantle boundary where differentiation produced floating plagioclase cumulates at the roof of magma chambers in Fe-rich, high-Al gabbroic liquids. Because of gravity, these floating plagioclase mush started to rise as diapirs through the crust and got emplaced into the mid–upper crust to form anorthosite plutons. By contrast, some workers believed that anorthosites were derived from the melting of the lower crust (e.g., Duchesne et al., 1999, and references therein). However, an experimental work (Longhi et al., 1999) followed by Re–Os isotope data (Schiellerup et al., 2000) supported a mafic lower crust origin for the anorthosite.

Selbekk and Skjerlie (2002) conducted water-saturated melting experiments on a nepheline-normative metagabbro sample 109SD from the Rognsund Intrusion within the

Seiland Igneous Province (Norway). They suggested that anorthosite liquids can form by anatexis of nepheline-normative mafic rocks in the presence of an H<sub>2</sub>O-bearing fluid phase. Krättli and Schmidt (2021) conducted piston-cylinder experiments using synthetic samples (stg3 + plag in the ratio 90:10 and 70:30) to investigate the role of gravitation and density differences for anorthosite formation from basaltic melts. Their experiments confirm that gravitational segregation of plagioclase is feasible to produce cumulates. Latypov et al. (2020) explored the formation of anorthosite in layered intrusions in the Bushveld Complex using thermodynamic modeling. Their input parameters were as follows: 1) starting composition as “B2 melt” (Barnes et al., 2010), which is a basaltic andesite melt enriched in Al<sub>2</sub>O<sub>3</sub>; 2)  $p = 1\text{--}10$  kbar; 3) oxygen buffer = QFM; and 4) H<sub>2</sub>O = 0.55 wt%. Their results showed that orthopyroxene is the first liquidus phase at  $p = 10\text{--}3$  kbar, whereas plagioclase is the first liquidus phase between 0 and 3 kbar. There is a plagioclase-only saturation field at  $T = \sim 1,200^\circ\text{C}$  and  $p = 1\text{--}3$  kbar (Latypov et al., 2020; Figure 5).

We attempted to model the formation of anorthosite in our study area using MELTS software, an Excel program downloaded from <http://melts.ofm-research.org/> (Gualda et al., 2012). Our input parameters were  $p = 3$  kbar,  $f_{\text{O}_2} = \text{QFM}$ , and H<sub>2</sub>O = 1 wt% with all phases included in the check box. Our first approach was to use the starting compositions such as 1) hornblendite, pyroxenite, and dolerite samples of this study; 2) basalt sample RJ 8 of Ahmad et al. (2021); and 3) gabbro sample B7 of Manikyamba et al. (2020). However, it was seen that plagioclase was not the first liquidus phase in any of these samples.

Our second approach was to use the starting compositions from Selbekk and Skjerlie (2002) and Krättli and Schmidt (2021). MELTS modeling showed that plagioclase was the first liquidus phase at 3 bar when samples of both Selbekk and Skjerlie (2002) and Krättli and Schmidt (2021) were used as the starting compositions. It was also seen that the liquid line of descents (LLDs) produced by sample stg3 + plag (Krättli and Schmidt, 2021) begin much closer to anorthosite than LLDs of sample 109SD (Selbekk and Skjerlie, 2002) (refer to Figure 8). This is more obvious in the LLD of Fe<sub>2</sub>O<sub>3</sub>(t), TiO<sub>2</sub>, and Al<sub>2</sub>O<sub>3</sub>. We, therefore, suggest that anorthosite of our study area may have crystallized from plagioclase-saturated basaltic melts at  $p = \sim 3$  kbar. The shape of LLDs produced by stg3 + plag also suggests that some of the gabbros, particularly of Rasheed et al. (2021), are products of residual melts generated after the crystallization of anorthosite.

We also performed crystallization modeling from 0.001 to 10 kbar using sample stg3 + plag (Krättli and Schmidt, 2021) to check for the generation of the plagioclase-only field in the P-T diagram. Sample stg + plag (70:30) produced plagioclase as the first liquidus phase at all pressures from  $p = 0.001\text{--}10$  kbar. However, sample stg + plag (90:10) produced plagioclase as the first liquidus phase from  $p = 0.001\text{--}6$  kbar, whereas clinopyroxene is the first liquidus phase from  $p = 6\text{--}10$  kbar

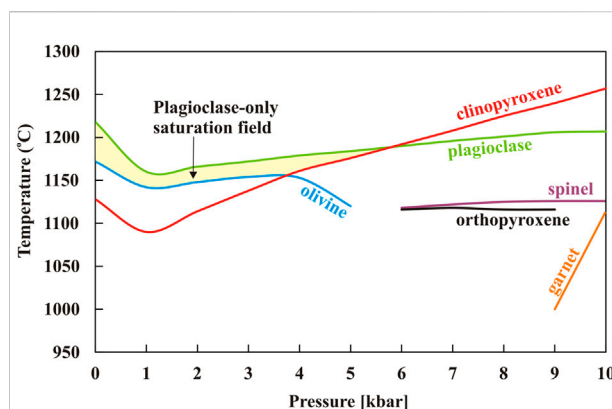


FIGURE 12

Temperature and pressure diagram (after Latypov et al., 2020) showing mineral saturation curves calculated by using sample stg3 + plag (90:10) from Krättli and Schmidt, (2021) as the starting composition in the MELTS program at oxygen buffer = QFM, H<sub>2</sub>O = 1 wt%, and  $p = 0.001\text{--}10$  kbar. Plagioclase-only saturation field is obtained between  $p = 0.001\text{--}6$  kbar shown by the yellow-filled area.

(Figure 12). These results support that anorthosite of the study area formed from the plagioclase-saturated basaltic melt.

## 6 Conclusion

The Proterozoic granites from the northern margin of the CGGC of Eastern India appear to have been intruded by multiple injections of magma and crystal mush into an oceanic island arc, forming granites. These granites host enclaves of anorthosite. These anorthosites in turn host pyroxenite, hornblendite, and diorite enclaves. All the enclaves have a sharp margin with the host rock and display variable dimensions and shapes from angular to subrounded bodies.

PM normalized WR trace element patterns of the anorthosites display near-parallel enrichment trends that increase from Lu to Rb, with moderate to strong positive anomalies at Y, Ti, Sr, and Pb. Host granite is slightly more enriched than anorthosite, with strong to moderate negative anomalies at Ti, P, Sr, Nb, and Ba and a moderate positive anomaly at Pb. Pyroxenite, hornblendite, diorite, and dolerite samples of this study display near-parallel enrichment trends that slightly increase from Lu to Rb.

Pressure and temperature of amphibole crystallization are constrained between 0.2 and 6.3 kbar and 635–807°C for pyroxenite, 0.2–6.6 kbar and 658–788°C for hornblendite, and 0.5–6.4 kbar and 653–780°C for anorthosite of the study area.

EDM modeling of anorthosites shows that the WR melt curves display a near-parallel and increasing trend from Gd to La with a negative anomaly at Eu. Parental melt curves calculated using the Nernst distribution coefficient equation show that melt compositions from Sm to La are near parallel and constrained broadly between TMF =  $\sim 5\text{--}15\%$ .

MELTS modeling shows that the anorthosite of our study area might have crystallized from plagioclase-saturated basaltic melts at  $p = \sim 3$  kbar. Crystallization modeling inferences show that the parental melt for anorthosite was generated at deeper levels, which then ascended adiabatically to shallower depths. At last, it caused the melt to become plagioclase saturated, resulting in crystallization and gravity flotation of plagioclase cumulates as enclaves within the Proterozoic granites of CGGC.

## Data availability statement

The original contributions presented in the study are included in the article/[Supplementary Material](#); further inquiries can be directed to the corresponding author.

## Author contributions

AS: field, data generation, and writing (lead); PN: field, data generation, and writing (supporting); MA: field and data generation (supporting); DU: LA-ICP-MS data generation (lead); SA: writing (supporting).

## Funding

This study is supported by funding from the University of Delhi, under the faculty research grant -IoE (IoE/FRP/PCMS/2020/27) to AS.

## References

- Acharyya, S. K. (2003). The Nature of Mesoproterozoic Central Indian tectonic zone with exhumed and reworked older granulites. *Gondwana Res.* 6, 197–214. doi:10.1016/s1342-937x(05)70970-9
- Ahmad, M., Paul, A., Negi, P., Akhtar, M. S., Saikia, A., and Gogoi, B. (2021). Mafic rocks with back-arc E-MORB affinity from the Chotanagpur granite gneiss complex of India: Relicts of a proterozoic ophiolite suite. *Geol. Mag.* 158, 1527–1542. doi:10.1017/s0016756821000078
- Balaram, V., Saxena, V. K., Manikyamba, C., and Ramesh, S. L. (1990). Determination of rare Earth elements in Japanese rock standards by inductively coupled plasma mass spectrometry. *A. T. Spectrosc.* 11, 19–23.
- Barbarin, B. (2005). Mafic magmatic enclaves and mafic rocks associated with some granitoids of the central Sierra Nevada batholith, California: Nature, origin, and relations with the hosts. *Lithos* 80, 155–177. doi:10.1016/j.lithos.2004.05.010
- Barnes, S. J., Maier, W. D., and Curl, E. (2010). Composition of the marginal rocks and sills of the rustenburg layered suite, Bushveld complex, south Africa: Implications for the formation of the platinum-group element deposits. *Econ. Geol.* 105, 1491–1511. doi:10.2113/econgeo.105.8.1491
- Bébién, J. (1991). "Enclaves in plagiogranite of the Guevgueli ophiolitic complex, Macedonia, Greece," in *Enclaves and granite petrology, Developments in petrology*. Editors J. Didier, and B. Barbarin (Amsterdam: Elsevier), 205–229.
- Bédard, J. H. (1994). A procedure for calculating the equilibrium distribution of trace elements among the minerals of cumulate rocks, and the concentration of trace elements in the coexisting liquids. *Chem. Geol.* 118, 143–153. doi:10.1016/0009-2541(94)90173-2
- Bédard, J. H. (2001). Parental magmas of the main plutonic suite anorthosites and mafic cumulates: A trace element modelling approach. *Contrib. Mineral. Pet.* 141, 747–771. doi:10.1007/s004100100268
- Bhowmik, S. K. (2019). The current status of orogenesis in the central Indian tectonic zone: A view from its southern margin. *Geol. J.* 54, 2912–2934. doi:10.1002/gj.3456
- Blundy, J. D., and Sparks, R. S. J. (1992). Petrogenesis of mafic inclusions in granitoids of the Adamello Massif, Italy. *J. Petrology* 33, 1039–1104. doi:10.1093/petrology/33.5.1039
- Cahill, J. T., Floss, C., Anand, M., Taylor, L. A., Nazarov, M. A., and Cohen, B. A. (2004). Petrogenesis of lunar highlands meteorites: Dhofar 025, dhofar 081, dar al Gani 262, and dar al Gani 400. *Meteorit. Planet. Sci.* 39, 503–529. doi:10.1111/j.1945-5100.2004.tb00916.x
- Chace, F. M. (1956). Abbreviations in field and mine geological mapping. *Econ. Geol.* 51, 712–723. doi:10.2113/gsecongeo.51.7.712
- Chappell, B. W., White, A. J. R., and Wyborn, D. (1987). The importance of residual source material (restite) in granite petrogenesis. *J. Petrology* 28, 1111–1138. doi:10.1093/petrology/28.6.1111
- Chappell, B. W. (1996). Magma mixing and the production of compositional variation within granite suites: Evidence from the granites of Southeastern Australia. *J. Petrol.* 37, 449–470. doi:10.1093/petrology/37.3.449
- Chappell, B. W., White, A. J. R., Williams, I. S., Wyborn, D., and Wyborn, L. A. I. (2000). Lachlan fold belt granites revisited: High- and low-temperature granites and

## Acknowledgments

AS and MA acknowledge the funding received from the University of Delhi, under the faculty research grant -IoE, (IoE/FRP/PCMS/2020/27). PN acknowledges University Grants Commission for JRF fellowship UGC ref no. 385/(CSIR-UGC-NET JUNE 2019).

## Conflict of interest

The authors declare that the research was conducted in the absence of any commercial or financial relationships that could be construed as a potential conflict of interest.

## Publisher's note

All claims expressed in this article are solely those of the authors and do not necessarily represent those of their affiliated organizations, or those of the publisher, the editors, and the reviewers. Any product that may be evaluated in this article, or claim that may be made by its manufacturer, is not guaranteed or endorsed by the publisher.

## Supplementary material

The supplementary material for this article can be found online at: <https://www.frontiersin.org/articles/10.3389/feart.2022.952554/full#supplementary-material>

- their implications. *Aust. J. Earth Sci.* 47, 123–138. doi:10.1046/j.1440-0952.2000.00766.x
- Chatterjee, N., Banerjee, M., Bhattacharya, A., and Maji, A. K. (2010). Monazite chronology, metamorphism–anatexis and tectonic relevance of the mid-Neoproterozoic Eastern Indian Tectonic Zone. *Precambrian Res.* 179, 99–120. doi:10.1016/j.precamres.2010.02.013
- Chatterjee, N., Crowley, J. L., and Ghose, N. C. (2008). Geochronology of the 1.55 Ga Bengal anorthosite and Grenvillian metamorphism in the Chotanagpur gneissic complex, eastern India. *Precambrian Res.* 161, 303–316. doi:10.1016/j.precamres.2007.09.005
- Chatterjee, N., and Ghose, N. C. (2011). Extensive early neoproterozoic high-grade metamorphism in north Chotanagpur gneissic complex of the central Indian tectonic zone. *Gondwana Res.* 20, 362–379. doi:10.1016/j.gr.2010.12.003
- Chen, Y. D., Price, R. C., and White, A. J. R. (1989). Inclusions in three S-type granites from southeastern Australia. *J. Petrology* 30, 1181–1218. doi:10.1093/ptetrology/30.5.1181
- Clemens, J. D., and Wall, V. J. (1988). Controls on the mineralogy of S-type volcanic and plutonic rocks. *Lithos* 21, 53–66. doi:10.1016/0024-4937(88)90005-9
- Clemens, J. D., and Wall, V. J. (1984). Origin and evolution of a peraluminous silicic ignimbrite suite: The violet town volcanics. *Contrib. Mineral. Pet.* 88, 354–371. doi:10.1007/bf00376761
- Dahlquist, J. A. (2002). Mafic microgranular enclaves: Early segregation from metaluminous magma (sierra de Chepes), pampean ranges, NW Argentina. *J. South Am. Earth Sci.* 15/6, 643–655. doi:10.1016/s0895-9811(02)00112-8
- Didier, J., and Barbarin, B. (1991). “Enclaves and granite petrology,” in *Developments in petrology*, 13. Amsterdam: Elsevier, 625.
- Dodge, F. C. W., and Kistler, R. W. (1990). Some additional observations on inclusions in the granitic rocks of the Sierra Nevada. *J. Geophys. Res.* 95, 17841–17848. doi:10.1029/jb095ib11p17841
- Donaire, T., Pascual, E., Pin, C., and Douthou, J. L. (2005). Microgranular enclaves as evidence of rapid cooling in granitoid rocks: The case of the los pedroches granodiorite, iberian massif, Spain. *Contrib. Mineral. Pet.* 149, 247–265. doi:10.1007/s00410-005-0652-0
- Dorais, M. J., Whitney, J. A., and Roden, M. F. (1990). Origin of mafic enclaves in the dinkey creek pluton, central sierra Nevada batholith, California. *J. Petrology* 31, 853–881. doi:10.1093/ptetrology/31.4.853
- Duchesne, J. C., Liégeois, J. P., Vander Auwera, J., and Longhi, J. (1999). The crustal tongue melting model and the origin of massive anorthosites. *Terra nova*. 11, 100–105. doi:10.1046/j.1365-3121.1999.00232.x
- Feeley, T. C., Wilson, L. F., and Underwood, S. J. (2008). Distribution and compositions of magmatic inclusions in the Mount Helen dome, Lassen Volcanic Center, California: Insights into magma chamber processes. *Lithos* 106, 173–189. doi:10.1016/j.lithos.2008.07.010
- Fershtater, G. B., and Borodina, N. S. (1991). “Enclaves in the hercynian granitoids of the ural mountains, U.S.S.R.,” in *Enclaves and granite petrology*. Editors J. Didier and B. Barbarin (Amsterdam, Newyork: Elsevier), 83–94.
- Fershtater, G. B., and Borodina, N. S. (1977). Petrology of autoliths in granitic rocks. *Int. Geol. Rev.* 19, 458–468.
- Floss, C., James, O. B., McGee, J. J., and Crozaz, G. (1998). Lunar ferroan anorthositic petrogenesis: Clues from trace element distributions in FAN subgroups. *Geochim. Cosmochim. Acta* 62, 1255–1283. doi:10.1016/S0016-7037(98)00031-3
- Frost, T. P., and Mahood, G. A. (1987). Field, chemical, and physical constraints on mafic-felsic magma interaction in the Lamarck Granodiorite, Sierra Nevada, California. *Geol. Soc. Am. Bull.* 99, 272–291. doi:10.1130/0016-7606(1987)99<272:fcapco>2.0.co;2
- Gale, A., Dalton, C. A., Langmuir, C. H., Su, Y., and Schilling, J. G. (2013). The mean composition of ocean ridge basalts. *Geochem. Geophys. Geosyst.* 14, 489–518. doi:10.1029/2012GC004334
- Ghose, N. C., Chatterjee, N., Mukherjee, D., Kant, R. W., and Saunders, A. D. (2008). Mineralogy and geochemistry of the bengal anorthosite massif in the Chotanagpur gneissic complex at the eastern Indian shield margin. *J. Geol. Soc. India* 72, 263–277.
- Ghose, N. C. (1992). Chhotanagpur gneiss-granulite complex, eastern India. Present status and future prospect. *Indian J. Geol.* 84, 100–121.
- Ghose, N. C. (1983). “Geology, tectonics and evolution of the Chhotanagpur granite gneiss complex, eastern India,” in *Recent researches in Geology* (New Delhi: Hindustan Publ Corp), 10, 211–247.
- Gualda, G. A., Ghorso, M. S., Lemons, R. V., and Carley, T. L. (2012). Rhyolite-MELTS: A modified calibration of MELTS optimized for silica rich, fluid-bearing magmatic systems. *J. Petrology* 53, 875–890. doi:10.1093/ptetrology/egr080
- Joy, K. H. (2013). “Trace elements in lunar plagioclase as indicators of source lithology,” in Lunar Planet Sci Conf. (abstract #1033) (The Woodlands, TX) <https://www.lpi.usra.edu/meetings/lpsc2013/pdf/1033.pdf>.
- Karmakar, S., Bose, S., Sarbadhikari, A. B., and Das, K. (2011). Evolution of granulite enclaves and associated gneisses from Purulia, Chhotanagpur Granite Gneiss Complex, India: Evidence for 990–940Ma tectonothermal event(s) at the eastern India cratonic fringe zone. *J. Asian Earth Sci.* 41, 69–88. doi:10.1016/j.jseaes.2010.12.006
- Kent, J. J., Brandon, A. D., Joy, K. H., Peslier, A. H., Lapen, T. J., Irving, A. J., et al. (2017). Mineralogy and petrogenesis of lunar magnesium granulitic meteorite Northwest Africa 5744. *Meteorit. Planet. Sci.* 52, 1916–1940. doi:10.1111/maps.12898
- Krättili, G., and Schmidt, M. W. (2021). Experimental settling, floatation and compaction of plagioclase in basaltic melt and a revision of melt density. *Contrib. Mineral. Pet.* 176 (30), 30–27. doi:10.1007/s00410-021-01785-6
- Krawczynski, M. J., Grove, T. L., and Behrens, H. (2012). Amphibole stability in primitive arc magmas: Effects of temperature, H<sub>2</sub>O content, and oxygen fugacity. *Contrib. Mineral. Pet.* 164, 317–339. doi:10.1007/s00410-012-0740-x
- Krishna, V., Prasad, R. N., Pandey, U. K., Chabria, T., and Saxena, V. P. (1996). “Rb–Sr geochronology of Chhotanagpur gneiss granulite complex around Kailashnathgufa area, Raigarh district, M.P.,” in Proceedings, National Symposium on Mass Spectrometry, VIII, Gwalior, Indian Society of Mass Spectrometry (Defence Research and Development Establishment), 445–447.
- Larocque, J., and Canil, D. (2010). The role of amphibole in the evolution of arc magmas and crust: The case from the jurassic bonanza arc section, vancouver island, Canada. *Contrib. Mineral. Pet.* 159, 475–492. doi:10.1007/s00410-009-0436-z
- Latypov, R., Chistyakova, S., Costin, G., Namur, O., Barnes, S., and Kruger, W. (2020). Monomineralic anorthosites in layered intrusions are indicators of the magma chamber replenishment by plagioclase-only-saturated melts. *Sci. Rep.* 10 (1), 3839. doi:10.1038/s41598-020-60778-w
- Ilbeyli, N., and Pearce, J. (2005). Petrogenesis of igneous enclaves in plutonic rocks of the central anatolian crystalline complex, Turkey. *Int. Geol. Rev.* 47, 1011–1034. doi:10.2747/0020-6814.47.10.1011
- Longhi, J., Auwera, J. V., Fram, M. S., and Duchesne, J. C. (1999). Some phase equilibrium constraints on the origin of Proterozoic (massif) anorthosites and related rocks. *J. Petrology* 40, 339–362. doi:10.1093/ptetroj/40.2.339
- Mahadevan, T. M. (2002). *Geology of Bihar and Jharkhand*. Bangalore: J Geol Soc India, 563.
- Maji, A. K., Goon, S., Bhattacharya, A., Mishra, B., Mahato, S., and Bernhardt, H. J. (2008). Proterozoic polyphase metamorphism in the Chhotanagpur Gneissic Complex (India), and implication for trans-continental Gondwanaland correlation. *Precambrian Res.* 162, 385–402. doi:10.1016/j.precamres.2007.10.002
- Manikyamba, C., Pahari, A., Santosh, M., Ray, J., Sindhuja, C. S., Subramanyam, K. S. V., et al. (2020). Mesoarchean gabbro-anorthositic complex from Singhbhum craton, India. *Lithos* 366–367, 105541. doi:10.1016/j.lithos.2020.105541
- Mazumdar, S. K. (1988). “Crustal evolution of the Chhotanagpur gneissic complex and the mica belt of Bihar,” in *Precambrian of eastern Indian shield*. Editor D. Mukhopadhyay (Banglore, India: Mem Geol Soc Ind), 8, 49–83.
- Mukherjee, D., and Ghose, N. C. (1998). “Conglomerate at the base of Bihar Mica Belt metasediments, Koderma district, Bihar and its stratigraphic significance,” in *Proceedings of national seminar on advancement of geological sciences in Bihar* (Patna: Geological Survey of India), 15–16.
- Mukherjee, S., Dey, A., Sanyal, S., and Sengupta, P. (2019). “Proterozoic crustal evolution of the Chotanagpur granite gneissic complex, Jharkhand-Bihar-West Bengal, India: Current status and future prospect,” in *Tectonics and structural Geology: Indian context*. Editor S. Mukherjee (Cham: Springer Geology International Publishing AG), 7–54.
- Namur, O., and Humphreys, M. C. S. (2018). Trace element constraints on the differentiation and crystal mush solidification in the skaergaard intrusion, Greenland. *J. Pet.* 59 (3), 387–418. doi:10.1093/ptetrology/egy032
- Nielsen, R. L., Ustunisik, G. K., Lange, A. E., Tepley, F. I., and Kent, A. J. (2020). Trace element and isotopic characteristics of plagioclase megacrysts in plagioclase ultraphyric basalts (PUB). *Geochem. Geophys. Geosyst.* 21. doi:10.1029/2019GC008638
- Niu, Y. (2004). Bulk-rock major and trace element compositions of abyssal peridotites: Implications for mantle melting, melt extraction and post-melting processes beneath mid-ocean ridges. *J. Pet.* 45 (12), 2423–2458. doi:10.1093/ptetrology/egh068
- Pandey, M., Pandit, D., Arora, D., Chalapathi Rao, N. V., and Pant, N. C. (2019). Analytical protocol for U-Th-Pb chemical dating of monazite using CAMECA SXFive EPMA installed at the mantle petrology laboratory, department of Geology, Banaras Hindu university, varanasi, India. *J. Geol. Soc. India* 93, 46–50. doi:10.1007/s12594-019-1119-7

- Papike, J. J., Fowler, G. W., and Shearer, C. K. (1997). Evolution of the lunar crust: SIMS study of plagioclase from ferroan anorthosites. *Geochim. Cosmochim. Acta* 61, 2343–2350. doi:10.1016/S0016-7037(97)00086-0
- Papike, J. J., Fowler, G. W., Shearer, C. K., and Layne, G. D. (1996). Ion microprobe investigation of plagioclase and orthopyroxene from lunar Mg-suite norites: Implications for calculating parental melt REE concentrations and for assessing postcrystallization REE redistribution. *Geochim. Cosmochim. Acta* 60, 3967–3978. doi:10.1016/0016-7037(96)00212-8
- Perugini, D., Poli, G., Christofides, G., and Eleftheriadis, G. (2003). Magma mixing in the sithonia plutonic complex, Greece: Evidence from mafic microgranular enclaves. *Mineral. Pet.* 78, 173–200. doi:10.1007/s00710-002-0225-0
- Phillips, G. N., Wall, V. J., and Clemens, J. D. (1981). Petrology of the strathbogie batholith: A cordierite-bearing granite. *Can. Mineral.* 19, 47–63.
- Platevoet, B., and Bonin, B. (1991). “Enclaves and mafic-felsic associations in the permian alkaline province of corsica, France: Physical and chemical interactions between coeval magmas,” in *Enclaves and granite petrology, developments in petrology*. Editors J. Didier and B. Barbarin (Amsterdam: Elsevier), 13, 191–204.
- Pradhan, V. R., Meert, J. G., Pandit, M. K., Kamenov, G., Gregory, L. C., and Malone, S. J. (2009). India’s changing place in global proterozoic reconstructions: A review of geochronologic constraints and paleomagnetic poles from the dharwar, Bundelkhand and marwar cratons. *J. Geodyn.* 50, 224–242. doi:10.1016/j.jog.2009.11.008
- Purohit, K. K., Mukherjee, P. K., Saini, N. K., Khanna, P. P., and Rath, M. S. (2006). Geochemical survey of stream sediments from upper parts of alaknanda, mandakini, bhilangana and bhagirathi catchments, garhwal himalaya. *Him. Geol.* 27 (1), 31–39. WIHG publication, Dehradun, India.
- Putirka, K. (2016). Amphibole thermometers and barometers for igneous systems and some implications for eruption mechanisms of felsic magmas at arc volcanoes. *Am. Mineral.* 101 (4), 841–858. doi:10.2138/am-2016-5506
- Rasheed, K., Sarma, D., Asokan, A., Dash, J., and Bhutani, R. (2021). A non-arc tectonic setting for the evolution of Archean gabbro anorthosite Complexes: Evidence from the Singhbhum Craton, eastern India. *Precambrian Res.* 363, 106250. doi:10.1016/j.precamres.2021.106250
- Ridolfi, F., and Renzulli, A. (2012). Calcic amphiboles in calc-alkaline and alkaline magmas: Thermobarometric and chemometric empirical equations valid up to 1130°C and 2.2 GPa. *Contrib. Mineral. Pet.* 163, 877–895. doi:10.1007/s00410-011-0704-6
- Ridolfi, F., Renzulli, A., and Puerini, M. (2010). Stability and chemical equilibrium of amphibole in calc-alkaline magmas: An overview, new thermobarometric formulations and application to subduction-related volcanoes. *Contrib. Mineral. Pet.* 160, 45–66. doi:10.1007/s00410-009-0465-7
- Rieder, M., Cavazzini, G., D’Yakovov, Y. S., Frank-Kamenetskii, V. A., Gottardi, G., Guoggenheim, S., et al. (1998). Nomenclature of the micas. *Can. Mineral.* 36, 905–912.
- Russell, S. S., Joy, K. H., Jeffries, T. E., Consolmagno, G. J., and Kearsley, A. (2014). Heterogeneity in lunar anorthosite meteorites: Implications for the lunar magma ocean model. *Phil. Trans. R. Soc. A* 372, 20130241. doi:10.1098/rsta.2013.0241
- Saikia, A., Gogoi, B., Ahmad, M., and Ahmad, T. (2014). Geochemical constraints on the evolution of mafic and felsic rocks in the Bathani volcanic and volcano-sedimentary sequence of Chotanagpur Granite Gneiss Complex. *J. Earth Syst. Sci.* 123, 959–987. doi:10.1007/s12040-014-0455-7
- Saikia, A., Gogoi, B., Ahmad, M., Kumar, R., Kaulina, T., and Bayanova, T. (2019). “Mineral chemistry, Sr-Nd isotope geochemistry and petrogenesis of the granites of Bathani volcano-sedimentary sequence from the northern fringe of Chotanagpur Granite Gneiss Complex of eastern India,” in *Geological evolution of the precambrian Indian shield*. Editor M. E. A. Mondal (Bern: Springer Nature, Society of Earth Scientists), 79–120.
- Saikia, A., Gogoi, B., Kaulina, T., Lialina, L., Bayanova, T., and Ahmad, M. (2017). “Geochemical and U–Pb zircon age characterization of granites of the Bathani volcano-sedimentary sequence, Chotanagpur granite gneiss complex, eastern India: Vestiges of the nuna supercontinent in the central Indian tectonic zone,” in *Crustal evolution of India and Antarctica: The supercontinent connection*. Editors N. C. Pant and S. Dasgupta (London: Geological Society), 233–252. Special Publication no. 457.
- Sial, A. N., Ferreira, V. P., Fallick, A. E., and Cruz, M. J. M. (1998). Amphibole-rich clots in calc-alkalic granitoids in the Borborema province, northeastern Brazil. *J. South Am. Earth Sci.* 11 (5), 457–471. doi:10.1016/S0895-9811(98)00034-0
- Saini, N. K., Mukherjee, P. K., Rath, M. S., Khanna, P. P., and Purohit, K. K. (2007). A proposed amphibolite reference rock sample (AMH) from Himachal Pradesh. *J. Geol. Soc. India* 69, 799–802.
- Sanyal, S., and Sengupta, P. (2012). Metamorphic evolution of the Chotanagpur granite gneiss complex of the east Indian shield: Current status. *Geol. Soc. Lond. Special Publ.* 365, 117–145. doi:10.1144/SP365.7
- Sarkar, A. N. (1988). “Tectonic evolution of the Chhotanagpur plateau and Gondwana basins in Eastern India: An interpretation based on supra-subduction geological processes,” in *Precambrian of the eastern Indian shield*. Editor D. Mukhopadhyay (Bangalore, India: Mem Geol Soc Ind), 8, 127–146.
- Schiellerup, H., Lambert, D. D., Prestvik, T., Robins, B., McBride, J. S., and Larsen, R. B. (2000). Re–Os isotopic evidence for a lower crustal origin of massif-type anorthosites. *Nature* 405, 781–784. doi:10.1038/35015546
- Selbekk, R. S., and Skjerlie, K. P. (2002). Petrogenesis of the anorthosite dyke swarm of tromso, north Norway: Experimental evidence for hydrous anatexis of an alkaline mafic complex. *J. Pet.* 43 (6), 943–962. doi:10.1093/petrology/43.6.943
- Sharma, R. S. (2009). “Cratons of the Indian shield,” in *Cratons and fold belts of India. Lecture notes in earth sciences* (Berlin, Heidelberg: Springer), 127. doi:10.1007/978-3-642-01459-8\_2
- Singh, Y., and Krishna, V. (2009). Rb–Sr geochronology and petrogenesis of granitoids from the Chhotanagpur granite gneiss complex of Raikera–Kunkuri region, Central India. *J. Geol. Soc. India* 74, 200–208. doi:10.1007/s12594-009-0122-9
- Sun, S. S., and McDonough, W. F. (1989). “Chemical and isotopic systematics of oceanic basalts: Implications for mantle composition and process,” in *Magmatism in the ocean basins*. Editors A. D. Saunders and M. J. Norry (London: Geol Soc Spec Publ), 42, 313–345.
- Vernon, R. H. (1984). Microgranitoid enclaves in granites-globules of hybrid magma quenched in a plutonic environment. *Nature* 309, 438–439. doi:10.1038/309438a0
- Waard, D. D., Duchesne, J. C., and Michot, J. (1974). “Anorthosites and their environment,” in *Géologie des Domaines Cristallins*. Editors J. Bellière and J. C. Duchesne (Liege: Centenaire Société Géologique de Belgique), 323.
- White, A. J. R., and Chappell, B. W. (1977). Ultrametamorphism and granitoid Genesis. *Tectonophysics* 43, 7–22. doi:10.1016/0040-1951(77)90003-8
- White, A. J. R., Chappell, B. W., and Wyborn, D. (1999). Application of the restite model to the deddick granodiorite and its enclaves—a reinterpretation of the observations and data of maas et al. (1997). *J. Pet.* 40, 413–421.
- Whitney, D. L., and Evans, B. W. (2010). Abbreviations for names of rock-forming minerals. *Am. Mineral.* 95 (1), 185–187. doi:10.2138/am.2010.3371
- Wiebe, R. A., Smith, D., Sturn, M., King, E. M., and Seckler, M. S. (1997). Enclaves in the cadillac mountain granite (coastal Maine): Samples of hybrid magma from the base of the chamber. *J. Petrology* 38, 393–423. doi:10.1093/ptroj/38.3.393
- Workman, R. K., and Hart, S. R. (2005). Major and trace element composition of the depleted MORB mantle (DMM). *Earth Planet. Sci. Lett.* 231, 53–72. doi:10.1016/j.epsl.2004.12.005
- Yadav, B. S., Wanjari, N., Ahmad, T., and Chaturvedi, R. (2016). Geochemistry and petrogenesis of Proterozoic granitic rocks from northern margin of the Chotanagpur Gneiss Complex (CGC). *J. Earth Syst. Sci.* 125, 1041–1060. doi:10.1007/s12040-016-0709-7
- Zane, A., and Weiss, Z. (1998). A procedure for classifying rock-forming chlorites based on microprobe data. *Rend. Fis. Acc. Lincei* 9 (1), 51–56. doi:10.1007/bf02904455